

# Droplet Microfluidics with Aqueous Two-Phase Systems for Cell Encapsulation and Drug Delivery

by

Niki Abbasi

Bachelor of Engineering, Ryerson University, 2016

A thesis

presented to Ryerson University

in partial fulfillment of the  
requirements for the degree of  
Master of Applied Science  
in the program of  
Mechanical and Industrial Engineering

Toronto, Ontario, Canada, 2018

©Niki Abbasi, 2018

## AUTHOR'S DECLARATION FOR ELECTRONIC SUBMISSION OF A THESIS

I hereby declare that I am the sole author of this thesis. This is a true copy of the thesis, including any required final revisions, as accepted by my examiners.

I authorize Ryerson University to lend this thesis to other institutions or individuals for the purpose of scholarly research

I further authorize Ryerson University to reproduce this thesis by photocopying or by other means, in total or in part, at the request of other institutions or individuals for the purpose of scholarly research.

I understand that my thesis may be made electronically available to the public.

# Droplet Microfluidics with Aqueous Two-Phase Systems for Cell Encapsulation and Drug Delivery

Master of Applied Science, 2018

Niki Abbasi

Mechanical and Industrial Engineering

Ryerson University

## **Abstract**

In this thesis, microfluidic platforms based on aqueous two-phase systems (ATPS) are developed. First, it is shown that exploiting affinity partitioning of particles, to the interface of an ATPS, enables the generation of particle stabilized water-in-water emulsions within a microfluidic platform. The process of droplet coverage is studied, and it is shown that the coverage of the droplets can be tuned by varying the size and the concentration of the particles used. Then, it is shown that integrating ionic cross-linking of alginate and calcium chloride, within the ATPS, can lead to the generation of spiky microparticles. The length of spikes on the microparticles can be tuned by changing the concentration of the calcium chloride solution. Particle-stabilized emulsions, and the spiky microparticles may have different biotechnological applications, for instance, for cell encapsulation, and drug delivery applications respectively.

## **Acknowledgements**

There are so many people who have had great positive impacts on me during all throughout my studies at Ryerson. First and foremost, I would like to thank my advisor, Dr. Scott S. H. Tsai, for his guidance, support and mentorship, throughout my undergraduate and graduate studies. His enthusiasm and scientific inquiry has taught me an appreciation for research, and its impact on life. My life's trajectory has changed for the better ever since I got to work at Laboratory of Fields, Flows, and Interfaces (LoFFI).

I would like to thank former LoFFI graduate student, Steven Jones, and former LoFFI post-doctorate fellow, Dr. Byeong-Ui Moon, for their tireless trainings and support at the lab, throughout my undergraduate studies I learned so much from them, and deeply enjoyed working with both of them from 2014- 2016.

From fourth year of undergraduate onwards, I have had the privilege of working with Maryam Navi, who has become one of my best friends, and greatest lab-partner. I have never had a dull moment with her. Our small discoveries and eureka moments, experimentations, and lab discussions have broadened my view and have made me a better person!

I would like to thank all current and former LoFFI personnel for all the great memories, from scientific discussions to celebrations, and also thank them all for their help and support throughout the past few years: Vaskar Gnyawali, Morteza Jeyhani, Huma Inayat, Jennifer Kieda, Stephanie Buryk, Ali Salari, Jiang Xu, Katherine Chan, Lianne So, Stephen Sammut, Ali Saremi, Nevetha Yogorajah, and Brian Battaglia.

Outside the lab, my close Ryerson friends, Ana Daniya, Farhan Riaz, Matthew Vassov, and Sarah Marshall have all helped me become a better person, and they have always been encouraging and supportive in difficult times. Words cannot express how grateful I am to all of them.

I gratefully acknowledge funding support from the Ontario Graduate Scholarship (OGS) program, which has assisted me with my graduate studies at Ryerson.

Last, but not least, I would like to thank my awesome family, my mom Soheila, my dad Mosi, and my brothers Milad and Hessam, for their support all throughout my studies. I would not have been able to do anything without them.

## **Dedication**

To my lovely grandparents, and parents.

# Table of Contents

<b>Abstract.....</b>	<b>iii</b>
<b>List of Figures.....</b>	<b>xii</b>
<b>Nomenclature .....</b>	<b>xiv</b>
<b>Chapter 1: Concepts and motivations.....</b>	<b>1</b>
1.1 Microfluidics.....	1
1.2 Droplet Microfluidics.....	3
1.3 Aqueous Two-Phase Systems.....	7
1.4 Overview of the Thesis.....	9
1.5 Author's Contribution.....	10
<b>Chapter 2: Microfluidic generation of particle-stabilized water-in-water emulsions .....</b>	<b>12</b>
2.1 Abstract.....	12
2.2 Introduction.....	13
2.3 Experimental methods .....	16
2.3.1 Chemicals.....	16
2.3.2 Microparticle suspension .....	17
2.3.3 Cells .....	17
2.3.4 Device fabrication.....	18
2.3.4 Experimental setup.....	19
2.4 Results and discussion .....	22
2.5 Conclusions.....	34
<b>Chapter 3: Spiky microparticle generation by integrating ionic cross-linking within an aqueous two-phase system.....</b>	<b>35</b>
3.1 Abstract.....	35
3.2 Introduction.....	36
3.3 Experimental methods .....	39
3.3.1 Chemical preparations .....	39
3.3.2 Device fabrication.....	41
3.3.3 Experimental setup.....	42
3.4 Results and discussion .....	44
3.5 Conclusions.....	52
<b>Chapter 4: Concluding remarks.....</b>	<b>53</b>
<b>Appendix.....</b>	<b>56</b>
A1. Order-of-Magnitude Approximations .....	56
Gibbs desorption free energy .....	56
Thermal energy.....	57
Stokes' drag-based shear energy.....	58
<b>Bibliography .....</b>	<b>59</b>

# List of Figures

- Figure 1.** Schematics of (a) T-junction and (b) flow-focusing droplet microfluidics systems. .... 4
- Figure 2.** The presence of the oil phase in typical water-in-oil droplet microfluidic platforms compromises the viability of biological cargo inside the droplets. Replacing the oil phase with a biocompatible aqueous solution resolves the challenges associated with conventional water-in-oil droplet microfluidics platforms..... 7
- Figure 3.** A representative binodal curve of two incompatible polymer solutions. The concentration combinations chosen below the binodal curve result in one homogeneous mixture, whereas concentration combinations chosen above the binodal curve result in two distinct phases. .... 8
- Figure 4.** (a) An inverted microscope and a high-speed camera are used to monitor experiments and record videos. (b) Experimental setup of the microfluidic system, with pipette tips inserted at the inlets for infusion of the fluids into the chip. (c) Schematic diagram of the microfluidic device. A patterned PDMS slab is bonded to a glass slide, using a plasma chamber. (d) Schematic diagram of the flow-focusing junction of the microfluidic device. The droplets are generated at a flow-focusing junction with an orifice. .... 21
- Figure 5.** Time-series images of DEX droplets being covered with  $d = 10 \mu\text{m}$  diameter carboxylated particles, at different particle concentrations, in the serpentine region of the microfluidic device. Higher particle concentrations result in faster coverage of the DEX droplets. Scale bar indicates  $50 \mu\text{m}$ . .... 23
- Figure 6.** Plot of droplet coverage  $Nd^2/4D^2$  versus carboxylated particle number concentration  $C$  in the PEG phase. The coverage of the DEX droplets increases with the particle concentration and particle size. Scale bars indicate  $50 \mu\text{m}$ . .... 28
- Figure 7.** (a) Plot of the final to initial droplet diameter ratio  $D_f/D_i$  versus droplet coverage  $Nd^2/4D^2$ . As expected, an increase in droplet coverage  $Nd^2/4D^2$  results in a decrease in the diameter ratio  $D_f/D_i$  indicating that droplets become stabilized against coalescence. (b) Plot of the final to initial droplet diameter  $D_f/D_i$  versus particle concentration  $C$ . (c) Inset shows a time-series of images of two particle-stabilized DEX droplets inside the reservoir of the microfluidic device. Despite being in contact over the course of 450 s, the two droplets do not coalesce. Scale bar indicates  $50 \mu\text{m}$ ..... 30
- Figure 8.** Time-series images of a particle-stabilized DEX droplet squeezing and flowing through a narrow constriction, which is located inside the reservoir of the microfluidic device. Stabilizing particles have diameter  $d = 10 \mu\text{m}$ . Most particles remain on the droplet as the droplet exits the narrow constriction and return to a spherical shape. The scale bar indicates  $50 \mu\text{m}$ . .... 31
- Figure 9.** Time series images of a single particle- stabilized DEX droplet encapsulating an AML cell. The particles are  $10 \mu\text{m}$  in diameter. Scale bar indicates  $20 \mu\text{m}$ . .... 32

**Figure 10.** Fluorescence images of (a) live and (b) dead cells stained with calcein AM (green) and ethidium homodimer-1 (red), respectively. (c) The addition of DEX to a suspension of cells in MEM does not reduce the viability of the AML cells. The lack of nutrients in the solution of 12.8 w/v% DEX in PBS may be the cause of the lower AML cells viability observed in (c). Scale bar indicates 50  $\mu\text{m}$ . ..... 33

**Figure 11.** Schematic diagram of the experimental setup. A flow-focusing microfluidic device is used to generate emulsions of DEX-alginate in the continuous phase of PEG. The DEX-alginate droplets, which are generated inside the outlet tubing, flow into a bath of PEG-CaCl<sub>2</sub> solution, for 30 s. Then, the flows of DEX-alginate and PEG are stopped, the outlet tubing is disconnected from the PEG-CaCl<sub>2</sub> bath, and the bath of PEG-CaCl<sub>2</sub> is placed on an inverted microscope, to observe the polymerization and growth of spikes across the DEX-alginate droplets over time. The scale bar indicates 50  $\mu\text{m}$ . ..... 43

**Figure 12.** Process of spike formation across a DEX-alginate droplet. a) The DEX-alginate droplet reaches the polymerization bath of PEG-CaCl<sub>2</sub>. Water molecules diffuse between the PEG-CaCl<sub>2</sub> solution, and the intermediate PEG phase, resulting in a homogeneous mixture. b) The DEX-alginate droplet goes out of equilibrium with its surrounding, so to reach a new equilibrium, water molecules from the DEX-alginate droplet migrate outside. c) Water molecules flow out from the DEX-alginate droplets in the form of fingers. The simultaneous ionic cross linking of alginate in the droplets and fingers, and the CaCl<sub>2</sub> in the surrounding PEG phase results in polymerization of the spiky DEX-alginate particles. .... 46

**Figure 13.** (a) Time-series images of a 30 w/v% DEX - 1 w/v% alginate droplet inside a bath of 20 w/v% PEG - 2 w/v% CaCl<sub>2</sub>. With increasing time, the droplet starts to polymerize, spikes form over its surface and grow until the spike growth reaches a stable length at time  $t = 100$  minutes. (b) The final-state images of DEX-alginate particles, in different polymerization baths. With a fixed 2 w/v% CaCl<sub>2</sub> concentration, the final spike length of particles decreases with increasing  $C_{PEG}$  inside the bath. Scale bars indicate 50  $\mu\text{m}$ . ..... 48

**Figure 14.** (a) Log-log plot of the normalized spike length  $l/d$  versus time  $t$ , for different polymerization bath compositions. Given fixed CaCl<sub>2</sub> concentration in the bath, as  $C_{PEG}$  increases, the final length of spikes observed across the DEX-alginate particles decreases. Further, the spikes' growth across the DEX-alginate particles reaches a plateau faster when surrounded by a more concentrated PEG in the bath. (b) Plot of normalized final spike length  $l_f/d$  versus PEG concentration in the polymerization bath  $C_{PEG}$ . The final spike length  $l_f/d$  decreases with the concentration of the PEG solution inside the bath. .... 51

# Nomenclature

## Chapter 1

Symbol	Meaning
$Re$	Reynolds number
$\rho$	Density
$u$	Flow speed
$l$	Length
$\mu$	Viscosity
$C$	Concentration
$t$	Time
$D$	Diffusion Coefficient
$x$	Position
$Ca$	Capillary number
$\gamma$	Interfacial tension

## Chapter 2

Symbol	Meaning
$\gamma$	Interfacial tension
$\mu_{DEX}$	DEX phase viscosity
$\mu_{PEG}$	PEG phase Viscosity
$T$	Temperature
$d$	Particle diameter
$d_c$	Critical Particle diameter
$d$	DEX droplet diameter
$D_f$	Final DEX droplet diameter
$D_i$	Initial DEX droplet diameter
$h$	Height of the microfluidic device
$C$	Particle concentration
$t$	Time
$\Delta G$	Gibbs desorption free energy
$\theta$	Contact angle
$k$	Boltzmann's constant
$u$	DEX droplet's flow speed

## Chapter 3

Symbol	Meaning
$C_{PEG}$	PEG concentration in the polymerization bath
$C_{CaCl_2}$	CaCl <sub>2</sub> concentration in the polymerization bath

$d$	DEX – alginate droplet diameter
$l$	Spike length
$l_f$	Final spike length
$t$	Time
$D$	Diffusion coefficient

# Chapter 1

## Concepts and motivations

### 1.1 Microfluidics

The field of microfluidics emerged about two decades ago with the rise of micro-electromechanical systems (MEMS) and advances in manufacturing micron scale features. This field has enabled the manipulation and study of flows at micron level scales,<sup>1,2</sup> and microfluidic devices have become more accessible as tools, with the advances in microfabrication techniques. In particular, the soft lithography technique developed by Xia and Whitesides in 1998<sup>3</sup> made this platform more available to researchers, resulting in expansive growth and a surge of this field ever since.

Microfluidic platforms offer advantages over traditional wet-bench setups. The amount of reagents needed to perform a specific chemical/biological analysis, inside a microfluidic chip, is far less than the amount required to achieve the same task within a macro-scale setup. The low reagent and power consumption would, in turn, make microfluidic devices more cost effective, compared to conventional wet-bench configurations, and also would reduce the amount of waste produced.<sup>4,5</sup> Moreover, depending on the application, the design of microfluidic devices can be versatile, allowing the integration of parallel operations within a single device.<sup>4,5</sup>

This field has given rise to so-called lab-on-a-chip systems, which are microfluidic devices that miniaturize chemical/biological syntheses and analyses within microchannels, that are only a few hundreds of microns wide.<sup>6</sup> With designing and engineering complex networks of microchannels, and integrating external components, researchers have already been able to show a full transformation of wet-bench setups into microscale setups. For instance, lab-on-a-chip systems have been designed to purify and analyze DNA/RNA samples.<sup>7,8</sup> Point-of-care diagnostics devices for analysis of physiological fluids at such small scales have been developed.<sup>9,10</sup> Furthermore, these devices have also been engineered and used for studying biological samples, such as cells, at a single cell resolution.<sup>11,12</sup>

Microfluidics has profoundly changed research and experimentation in the fields of biotechnology and biomedicine. The physics of flows at micron scales has enabled biologists to conduct experiments and study a variety of biological entities within microfluidic channels, which mimic the real physiological environment of these samples.<sup>13,14</sup> For instance, it has been shown that microfluidic devices could be used to study blood-cell mass transport and cell glucose intake within microfluidic channels, which mimic the capillary vessels within human body.<sup>15</sup>

The physics of flows in microscale is rather different compared to flows in macroscale, and this can be captured by studying dimensionless numbers in the field of fluid mechanics. For instance, considering Reynolds number  $Re = \rho ul / \mu$  in microscale, where  $\rho$  represents fluid density,  $u$  is flow speed,  $l$  represents the hydraulic diameter of the microchannel, and  $\mu$  is the fluid viscosity, it

is observed that the viscous effects are much greater than inertial effects in microfluidic platforms, resulting in viscosity dominated Stokes flows inside microchannels.<sup>4,16</sup>

Besides the major role of viscosity, diffusion also becomes an essential driving force for transfer of biological molecules, particles and cells within microfluidic platforms. Based on Fick's second law of diffusion,  $\frac{\partial C}{\partial t} = D \frac{\partial^2 C}{\partial x^2}$ , where  $C$  is concentration,  $t$  represents time,  $D$  is the diffusion coefficient, and  $x$  is the position, it can be inferred that  $x^2 \approx Dt$ , which in turn means that the transfer of molecules in microchannels is going to be much faster, therefore resulting in efficient mass transport, compared to conventional bulk experiments.<sup>13,16</sup> Another factor that becomes prominent in the micron scale is the importance of the surface area. The micron length scale would result in a high surface area to volume ratio, which effectively enhances adsorption and/or diffusion of molecules to/from materials within microfluidic platforms.<sup>17</sup>

## 1.2 Droplet Microfluidics

Droplet microfluidics, which is a sub-category of microfluidics, involves the generation of discrete monodisperse droplets, that are only a few microns in diameter, using immiscible fluids.<sup>18-20</sup> Compared to continuous-flow microfluidic platforms, droplet microfluidics provide more control and versatility, enabling analyses to be done within droplets and moreover, allowing for processes to be scaled up easier.<sup>18</sup>

To generate the droplets, either T-junction, or flow-focusing microfluidic designs can be used. As seen in Figure 1(a), a T-junction configuration is a microfluidic channel design in which the channel containing the droplet phase (also known as the dispersed phase), intersects with the channel that contains the fluid which surrounds the droplet phase (known as the continuous phase).<sup>21–23</sup> The flow-focusing configuration, on the other hand, is a symmetric design in which two streams of the continuous phase shears the dispersed phase, resulting in droplet generation (Figure 1(b)).<sup>24,25</sup>

In flow focusing configurations, droplets form in the continuous phase as the shear stress applied from the continuous phase to the dispersed phase overcomes the interfacial stress. The droplet pinch-off in any microfluidic system can be characterized by studying the dimensionless Capillary number  $Ca = \frac{\mu u}{\gamma}$ , which demonstrates the effect of viscous forces to surface tension forces, where  $\mu$  is the dynamic viscosity of the continuous phase,  $u$  is the velocity of the continuous phase, and  $\gamma$  is the interfacial tension.<sup>18,25</sup>

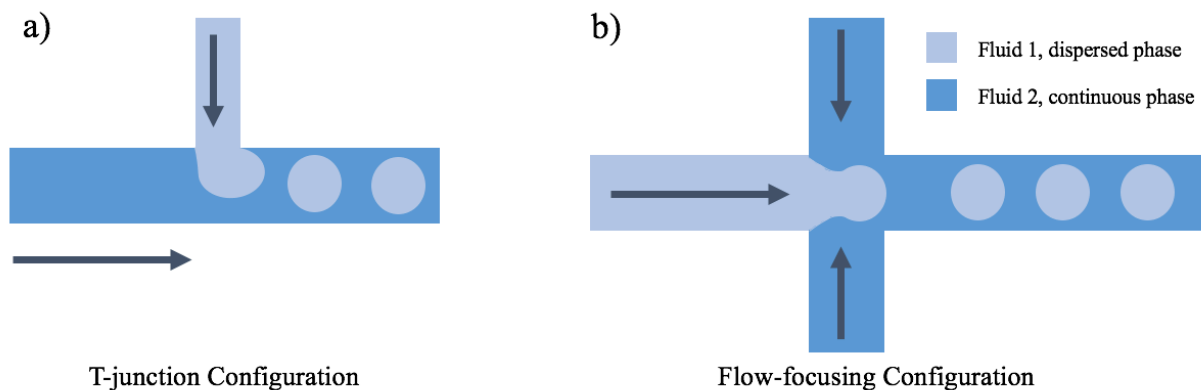


**Figure 1.** Schematics of (a) T-junction and (b) flow-focusing droplet microfluidics systems.

Droplet microfluidic platforms have been used in a wide range of applications, such as developing droplet-based micro-reactors for chemical synthesis,<sup>26</sup> for encapsulation and single-cell analysis,<sup>27–29</sup> development of synthetic biological samples, such as artificial cells<sup>30,31</sup>, and creating therapeutic and drug delivery vehicles.<sup>32,33</sup> Spherical<sup>34</sup> and non-spherical microparticles,<sup>35</sup> hollow microcapsules,<sup>36</sup> and double emulsions<sup>37</sup> (which are droplets containing smaller droplet compartments inside), have been engineered for encapsulation and delivery purposes.

To prevent the droplets from coalescing (merging), chemical surfactants,<sup>38</sup> or colloidal particles<sup>39</sup> can be used to stabilize the droplets against coalescence. Moreover, transforming the droplets to solid particles through ionic cross-linking of two different ionic compounds (such as alginate and calcium ions),<sup>40,41</sup> or UV polymerization (triggering polymerization by shining UV light to a droplet containing photo-initiator),<sup>42</sup> also results in the stabilization of these carriers.

Conventionally, water-in-oil systems are used to create droplets within microfluidic platforms. Water and oil phases are pumped through a tubing into the microfluidic platforms, and as the water and oil phase meet at the junction of the microfluidic platform, water droplets form readily, surrounded by the oil phase. The high interfacial tension of water-oil systems allows for easy and high throughput generation of discrete water droplets, surrounded by the oil phase, without any external perturbation of the interface between the two phases.<sup>18</sup> For a variety of biotechnological applications, reagents and samples would be pre-mixed with the dispersed phase of water, and the resulting water droplets would be enriched with the samples.

Although water-in-oil droplets can be easily generated, they possess a significant drawback, and that is the toxicity of the oil phase surrounding the aqueous droplet phase.<sup>43</sup> For the case of cellular microencapsulation, the presence of the oil phase around the droplets does not allow for diffusion of oxygen and nutrients to the droplet, affecting the viability of biological samples, that are present inside the droplet (see Figure 2). Furthermore, for delivery applications to targeted cells and tissues, these microcapsules also need to be washed to remove the continuous oil phase. This post-processing washing step may be carried out outside the microfluidic device, by collecting the sample and centrifuging it in bulk,<sup>40</sup> or, it can be incorporated within the microfluidic device. For instance, Deng *et al.*<sup>44</sup> combined side branches, containing aqueous solutions, to the droplet microfluidics platform to move hydrogel beads from the oil phase to the aqueous phase. Extraction chambers have been used to isolate gelled microspheres from the toxic oil phase and subsequently introduce the cell-containing gelled microspheres to a culture medium.<sup>45</sup> Post-processing by washing is cumbersome, and may affect and compromise the viability of biological samples encapsulated inside the droplet phase.

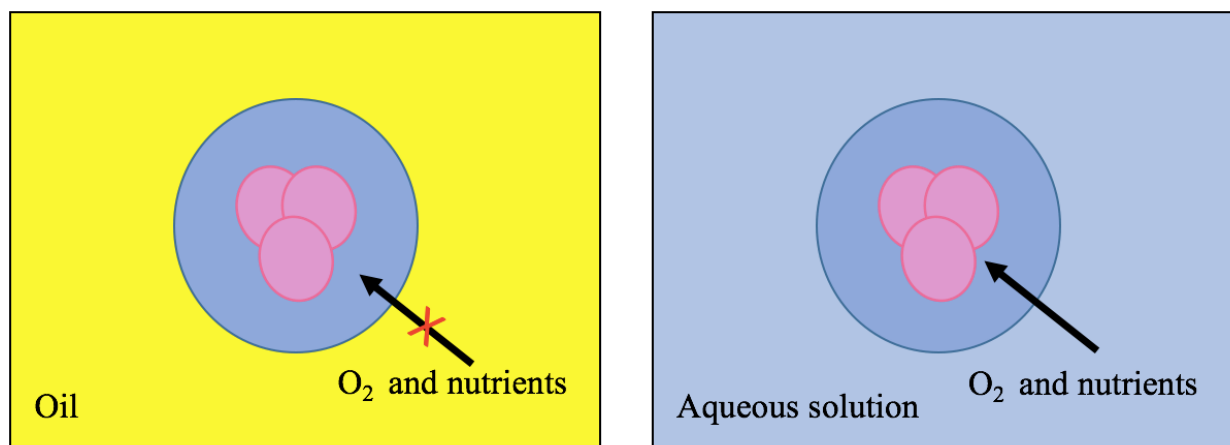


**Figure 2.** The presence of the oil phase in typical water-in-oil droplet microfluidic platforms compromises the viability of biological cargo inside the droplets. Replacing the oil phase with a biocompatible aqueous solution resolves the challenges associated with conventional water-in-oil droplet microfluidics platforms.

### 1.3 Aqueous Two-Phase Systems

Water in-water systems have shown to be a promising and powerful substitute to conventional water-in-oil systems within microfluidic platforms. The mild and biocompatible nature of these aqueous two-phase systems (ATPS) makes these systems a great to substitute to typical water-in-oil systems, removing the necessary post-processing washing steps needed for water-in-oil systems,<sup>46</sup> and realizing the full potential of droplet microfluidic platforms for biotechnological applications. The droplet microfluidics community, realizing the great potential of these all aqueous systems, has started to integrate ATPS within droplet microfluidic platforms for a variety of biotechnological applications.

ATPS is a mixture of two different and incompatible polymeric solutions,<sup>47</sup> which has traditionally been used for separation and partitioning of different biological samples, such as particles,<sup>48</sup> proteins,<sup>49,50</sup> and cells,<sup>51,52</sup> based on their affinity to each phase. Some of the factors which may affect the affinity partitioning of samples within ATPSs are the molecular weight and concentration of the polymers,<sup>53</sup> and the difference in hydrophobicity of the two polymeric solutions.<sup>54</sup> For instance, Albertsson has reported that proteins tend to favor the aqueous polymer phase with lower molecular weight.<sup>53</sup> Furthermore the importance of hydrophobicity of samples, and their correlation to the hydrophobicity of the phase to which they mostly partition to has been studied extensively. Specifically, it has been observed that hydrophobic materials tend to partition to phases which are more hydrophobic, and hydrophilic samples tend to partition to phases which are hydrophilic.<sup>54</sup>

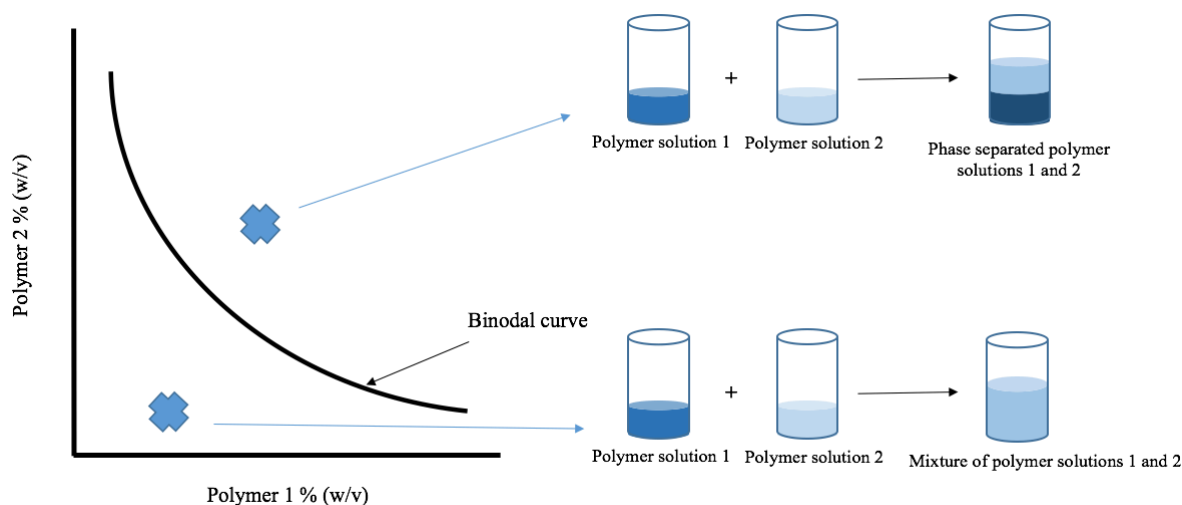


**Figure 3.** A representative binodal curve of two incompatible polymer solutions. The concentration combinations chosen below the binodal curve result in one homogeneous mixture, whereas concentration combinations chosen above the binodal curve result in two distinct phases.

These all-aqueous systems are characterized by binodal curves, as seen representatively in Figure 3. The binodal curve shows that if the chosen concentrations of the two polymer solutions were below the binodal curve, the mixture of the two polymer solutions results in a homogeneous one-phase solution. However, if the concentration combinations are chosen above the binodal curve, then the polymeric solutions phase separate, resulting in two distinct phases. The polymer solution with the higher density forms at the bottom, whereas the less dense one forms at the top. So, to utilize water-in-water droplets within microfluidic platforms, one needs to choose concentration combinations above the binodal curve, so that two distinct phases are formed, separated by a liquid-liquid interface.

## 1.4 Overview of the Thesis

In this thesis, ATPSs are used for developing lab-on-a-chip platforms, and generating new materials, towards biotechnological applications. Careful tunings of chemical compositions within ATPS, and utilizing affinity partitioning of particles and chemical compounds within these systems, can lead to development of stabilized water-in-water droplet microfluidic platforms, which may have applications for cell encapsulation. Moreover, coupling nonequilibrium ATPSs with ionic cross-linking enables generation of spiky microparticles, which may have applications as drug delivery vehicles.

In Chapter 2 of this thesis, it is shown that exploiting the affinity partitioning of colloidal particles to the interface of an ATPS can lead to generation of water-in-water emulsions that are stable against coalescence. These particle-stabilized carriers can then be used for the encapsulation of

different biological samples. Specifically, the process of droplet stabilization using colloidal particles, within a microfluidic platform, is studied, and the coverage and stability of these all-aqueous droplets are analyzed. The work presented in Chapter 2 is based on the following article published in a peer reviewed journal *Langmuir*.

*Abbasi, N., Navi, M., Tsai, S. S. H. (2018). Microfluidic generation of particle-stabilized water-in-water emulsions. Langmuir, 34 (1), 213-218. DOI: 10.1021/acs.langmuir.7b03245*

Then, in Chapter 3, it is shown that integrating ionic cross-linking within an ATPS allows for generation of spiky microparticles, which can be used for drug delivery applications. The process of spike formation on the surface of the droplets is studied, and the correlation of the spike length with experimental parameters is analyzed. The work presented Chapter 3 is based on a manuscript, which is in preparation for submission to a peer reviewed journal *Nature Materials*.

*Abbasi, N., Navi, M., Tsai, S. S. H. (2018). Spiky microparticle generation by integrating ionic cross-linking within an aqueous two-phase system*

## 1.5 Author's Contribution

The work presented in Chapter 2, Microfluidic generation of particle-stabilized water-in-water emulsions, was initiated by the author and Dr. Scott S. H. Tsai. The microfluidic device was fabricated by the author and Maryam Navi, and the experimental setup was designed by the author.

The chemicals were prepared by the author. The experiments, and data analyses were conducted by the author. The author, Maryam Navi and Dr. Scott S. H. Tsai all contributed to discussing the results.

As for Chapter 3, the work of generating spiky microparticles by ionic cross-linking within an aqueous two-phase system was initiated by the author and Dr. Scott S. H. Tsai. The microfluidic device was fabricated by Maryam Navi. The chemicals preparation and experimental setup design was done by the author. The author performed the experiments and analyzed the data. The author, Maryam Navi and Dr. Scott S. H. Tsai all contributed to discussing the results.

# Chapter 2

## Microfluidic generation of particle-stabilized water-in-water emulsions

The work presented in this chapter is based on the following article published in a peer reviewed journal *Langmuir*.

Abbasi, N., Navi, M., Tsai, S. S. H. (2018). Microfluidic generation of particle-stabilized water-in-water emulsions. *Langmuir*, 34 (1), 213-218. DOI: 10.1021/acs.langmuir.7b03245

### 2.1 Abstract

Herein, a microfluidic platform for generating particle-stabilized water-in-water emulsions is presented. The water-in-water system used is based on an aqueous two-phase system of polyethylene glycol (PEG) and dextran (DEX). DEX droplets are formed passively, in the continuous phase of PEG and carboxylated particle suspension, at a flow focusing junction inside a microfluidic device. As DEX droplets travel downstream inside the microchannel, carboxylated particles that are in the continuous phase partition to the interface of the DEX droplets, due to their affinity to the interface of PEG and DEX. As the DEX droplets become covered with carboxylated

particles, they become stabilized against coalescence. The coverage and stability of the emulsions, while tuning the concentration and the size of the carboxylated particles, are studied downstream inside the reservoir of the microfluidic device. These particle-stabilized water-in-water emulsions showcase good particle adsorption under shear, while being flowed through narrow microchannels. The intrinsic biocompatibility advantages of particle-stabilized water-in-water emulsions make them a good alternative to traditional particle-stabilized water-in-oil emulsions. To illustrate a biotechnological application of this platform, a proof-of-principle of cell encapsulation using this system is shown, which with further development, may be used for immunoisolation of cells for transplantation purposes.

## 2.2 Introduction

Using colloidal particles to stabilize droplets against coalescence was first reported in the early 1900s.<sup>55,56</sup> Since then, particle-stabilized emulsions (so-called Pickering Emulsions) have been exploited in a variety of different fields. Some of the biotechnological applications of particle-stabilized emulsions include drug encapsulation and drug delivery.<sup>57-59</sup> The deposition of particles onto liquid-liquid interfaces is also utilized for the realization of new structures and materials. For example, hollow colloidosomes, based on water-in-oil emulsions, are produced to serve as immunoisolation agents,<sup>60,61</sup> and porous silica is made by using stabilized emulsions as a template.<sup>62</sup> Particle-stabilization of both oil-in-water and water-in-oil emulsions is studied extensively, and particles based on iron,<sup>63</sup> protein,<sup>64</sup> silica,<sup>65</sup> latex,<sup>66</sup> and cellulose<sup>67</sup> are all effective stabilizing agents for oil-in-water and water-in-oil systems.

The conventional method of producing particle-stabilized emulsions is bulk emulsification, which involves mixing and stirring immiscible liquids with colloidal particles. This method of emulsification results in the generation of highly polydisperse droplets with different degrees of coverage, thus making it an unsuitable method for size-controlled emulsification.<sup>68</sup>

The advent of microfluidics in the past two decades is enabling the generation of highly monodisperse and functionalized water-in-oil and oil-in-water emulsions in a controlled fashion.<sup>21,24,69</sup> As a result, researchers are using microfluidics to generate monodisperse particle-stabilized emulsions.<sup>70-72</sup>

However, due to the toxicity of the organic oil phase, traditional particle-stabilized water-in-oil emulsions are not suitable for direct use in biotechnological applications, such as immunoisolation and drug delivery. An additional washing step is required to remove the oil phase from the particle-stabilized droplets, prior to their use.<sup>60,73</sup> For example, in the generation of hollow colloidosomes, the water-in-oil emulsions are washed and then transferred to an aqueous environment.<sup>60</sup> Although washing with an oil-soluble solution lightens the toxicity of the system, the shear stress caused by the washing flow may damage the assembly and the fine structure of the colloidal particles on the interface.<sup>73</sup>

Replacing the toxic organic continuous phase with a biocompatible fluid helps to eliminate the washing steps. This is a major reason why particle-stabilized water-in-water emulsions are desirable. Such water-in-water emulsions are based on aqueous-two-phase systems (ATPS), which

are comprised of two incompatible polymeric aqueous solutions. ATPS have been traditionally used as separation platforms for cells and macromolecules, based on their affinity partitioning and biocompatibility.<sup>74</sup> The mild environment of ATPS, which is due to their high water content, helps maintain the viability of biological samples.<sup>75–78</sup> The biocompatibility of ATPS makes them suitable candidates for making particle-stabilized emulsions for biotechnological applications.

Nevertheless, the ultra-low interfacial tension of ATPS makes it challenging to generate water-in-water emulsions using conventional microfluidic platforms, where syringe pumps are used to introduce the solutions.<sup>79</sup> As a result, a variety of active methods are proposed to realize microfluidic generation of water-in-water emulsions.<sup>80–85</sup> Recently, our group also introduced a passive microfluidic platform, that exploits the weak hydrostatic pressure difference of fluid columns from liquid-filled pipette tips inserted at the inlets of the dispersed and the continuous phases, to generate water-in-water droplets.<sup>86</sup>

In addition to generating water-in-water emulsions, realization of particle-stabilized water-in-water emulsions depends on the affinity of the selected particles to the fluid-fluid interface. The partitioning of particles within an ATPS depends highly on the surface interaction between the particles and the two aqueous phases. For example, emulsions of dextran-in-methylcellulose and dextran-in-polyethylene oxide can be stabilized by fat<sup>73</sup> and protein particles,<sup>87,88</sup> respectively, using bulk emulsification. Recently, Tsukamoto *et al.* reported affinity partitioning of carboxylated particles to the interface of an ATPS of polyethylene glycol (PEG) and dextran (DEX) within a microfluidic co-flow system.<sup>48</sup>

In this chapter, passive microfluidic platform<sup>86</sup> and the recently demonstrated affinity partitioning of carboxylated particles in the ATPS of PEG and DEX is utilized,<sup>48</sup> to generate particle-stabilized water-in-water emulsions. This is the first microfluidic implementation to generate particle-stabilized water-in-water emulsions. DEX droplets are formed at a flow focusing junction, in a continuous phase of PEG and carboxylated particles. As the DEX droplets travel downstream, carboxylated particles gradually cover the outer surface of the droplets by partitioning to the interface of the PEG and DEX phases. The effects of the size and concentration of the carboxylated particle suspension, on the coverage and stability of the particle-stabilized DEX droplets, is studied. Finally, it is shown that the particle-stabilized water-in-water emulsions can be used to encapsulate cells, demonstrating the potential biotechnological application of this approach for cellular immunoisolation.

## 2.3 Experimental methods

### 2.3.1 Chemicals

To prepare the ATPS, the protocol developed by Atefi *et al.*<sup>89</sup> is followed. Stock solutions of PEG 10 w/v% (PEG;  $M_w$  35k, Sigma Aldrich, St. Louis, MO, USA) and DEX 12.8 w/v% (DEX,  $M_w$  500k, Pharmacosmos, Holbaek, Denmark) are prepared in deionized (DI) water. These two stock solutions are mixed together inside a Falcon<sup>TM</sup> tube (BD Medical, Franklin Lakes, NJ, USA) and the mixture is left to phase separate over a course of 24 hours. Then, the top phase (equilibrated PEG phase) and bottom phase (equilibrated DEX phase) are separated and transferred to separate Falcon<sup>TM</sup> tubes, using syringes (BD Medical, Franklin Lakes, NJ, USA). The interfacial tension

of the ATPS, as reported by Atefi *et al.*,<sup>89</sup> is  $\gamma = 0.082 \text{ mN m}^{-1}$ . The dynamic viscosities of the DEX and PEG phase are  $\mu_{DEX} = 65.1 \text{ mPa s}$  and  $\mu_{PEG} = 15.0 \text{ mPa s}$ , respectively at room temperature ( $T = 20^\circ\text{C}$ ).<sup>90</sup>

### 2.3.2 Microparticle suspension

To make our particle suspension, Polybead® carboxylate microsphere solutions of diameter  $d = 1$ ,  $d = 6$  and  $10 \text{ }\mu\text{m}$  (Polysciences, Inc., Warrington, PA, USA) are used. Based on the particle solutions' data sheet, these carboxylated particles are negatively charged. To prepare the particle solution, 1 and  $10 \text{ }\mu\text{L}$  of the  $d = 1 \text{ }\mu\text{m}$  diameter carboxylated microsphere, 10.8, 86.6, 108 and  $173 \text{ }\mu\text{L}$  of the  $d = 6 \text{ }\mu\text{m}$  diameter carboxylated microsphere solution, and 50, 100, 200 and  $600 \text{ }\mu\text{L}$  of the  $d = 10 \text{ }\mu\text{m}$  diameter carboxylated microsphere solution, are added to 1 mL of phase separated PEG inside a safe-lock tube (Eppendorf, Hamburg, Germany) separately. After vigorously mixing the particles with PEG, the particle suspensions are centrifuged, and the carrier liquid is removed using a pipette. Then, 1 mL of phase separated PEG is added to the washed carboxylated particles to complete the particle suspensions. These different microparticle suspensions are used in order to observe the effect microparticles' size and concentration on the coverage and the stability of the DEX droplets.

### 2.3.3 Cells

Acute Myeloid Leukemia (AML) cells are used in cell encapsulation experiments. Cells are cultured in Minimum Essential Medium (MEM) with 10% fetal bovine serum (FBS). After culture, cells are incubated inside a T-25 flask, at  $37^\circ\text{C}$  with 5%  $\text{CO}_2$ . After a day of incubation, cells are

taken out from the T-25 flask (Thermo Scientific, Waltham, MA, USA) and transferred to a Falcon™ tube. Next, the cells are centrifuged to form a pellet at the bottom of the Falcon™ tube. Finally, after discarding the MEM solution, the cells are re-suspended in 1 mL of phase separated DEX solution.

To demonstrate the biocompatibility of the ATPS, a live/dead viability/cytotoxicity kit (LIVE/DEAD® viability/cytotoxicity kit for mammalian cells, Molecular Probes™, Eugene, OR, USA) is used to label AML cells. The viability of AML cells is monitored for up to 48 hours, in three different environments: Minimum Essential Medium (MEM Alpha 1×, Gibco® by Life Technologies™, Carlsbad, CA, USA) with 10 v/v% fetal bovine serum (FBS, Wisent Inc., QC, Canada), 12.8 w/v% DEX in MEM and FBS, and 12.8 w/v% DEX in phosphate buffered saline (PBS, MULTICELL, Wisent Inc., QC, Canada). AML cells are first cultured in MEM, with 10 v/v% FBS. After culture, the cell suspension is divided between three different flasks, media is removed from all three flasks, and the cells are seeded in fresh media, 12.8 w/v% DEX in MEM and 12.8 w/v% DEX in PBS, respectively. Using the protocol provided by Molecular Probes™, AML cells from each flask are stained with calcein and ethidium homodimer-1, and view the cell samples under fluorescence microscope.

### 2.3.4 Device fabrication

Standard soft lithography technique is used to make microfluidic devices.<sup>3</sup> To make a patterned photomask, microchannel design is prepared on a computer-aided design (CAD) software

(AutoCAD 2016, Autodesk, Inc., San Rafael, CA, USA) and then, the design is printed on a transparency sheet (CAD/ART Services Inc., Bandon, OR, USA).

To fabricate the microchannel features, a 4-inch diameter silicon wafer (UniversityWafer, Inc., Boston, MA, USA) is used. SU-8 2050 photoresist (Microchem, Newton, MA, USA) is spin-coated on the silicon wafer. The spin-coated wafer is exposed to UV light through the patterned photomask, to create the microchannel patterns. At the end, the unexposed photoresist is removed by washing the wafer with a developer solution, to complete the fabrication of the silicon master mold.

The silicon master mold is filled with a 10:1 ratio mixture of polydimethylsiloxane (PDMS) resin to curing agent (Sylgard 184, Dow Corning, Midland, MI, USA), and left in the oven to cure for 2 hours. Then, the PDMS slab is cut from the master, and 1 mm and 4 mm diameter biopsy punches (IntegraMiltex, Inc., Riethem-Weilheim, Germany) are used for making inlets and outlet, respectively. To complete the device fabrication, oxygen plasma treatment (Harrick Plasma, Ithaca, NY, USA) is used in order to bond the PDMS slab to a glass slide.

### 2.3.4 Experimental setup

Experimental images and videos are captured using an inverted microscope (IX71, Olympus Corp., Tokyo, Japan) with a connected high-speed camera (Miro M110, Vision Research, Wayne, NJ, USA) (Figure 4 (a)). ImageJ<sup>TM</sup> software is used to process videos and images.

A passive water-in-water droplet generation approach is used to infuse the liquids into the microfluidic device, and to make emulsions.<sup>86</sup> DEX, and the suspension of carboxylated particles in PEG, are filled into separate 200  $\mu\text{L}$  pipette tips, and subsequently inserted into their respective inlets on the microfluidic device (Figure 4(b)). The liquid column heights used for DEX, and the solution of PEG and suspended carboxylated particles, are 2.5 and 3.5 cm, respectively. This set of column heights is selected to ensure hydrostatic pressures that cause generation of monodisperse DEX droplets in the dripping regime. The flow speed established is also low enough to lead to the partitioning of carboxylated particles to the surface of the DEX droplets within the microfluidic device.

As seen in Figure 4(c), the microfluidic device is comprised of two inlets and one outlet. The inlet channels converge at a flow focusing junction, and connect to the main channel through an orifice, which is 30  $\mu\text{m}$  wide. The main channel, which is a long serpentine channel, is connected to a large circular reservoir near the outlet. All channel heights  $h = 50 \mu\text{m}$ . The flow of the DEX phase converges with the flow of the suspension of carboxylated particles in PEG, and DEX droplets with a diameter of  $D = 50 \mu\text{m}$  are generated (Figure 4(d)). As DEX droplets travel downstream through the serpentine channel, carboxylated particles in the continuous phase gradually partition to the outer surface of the DEX droplets.

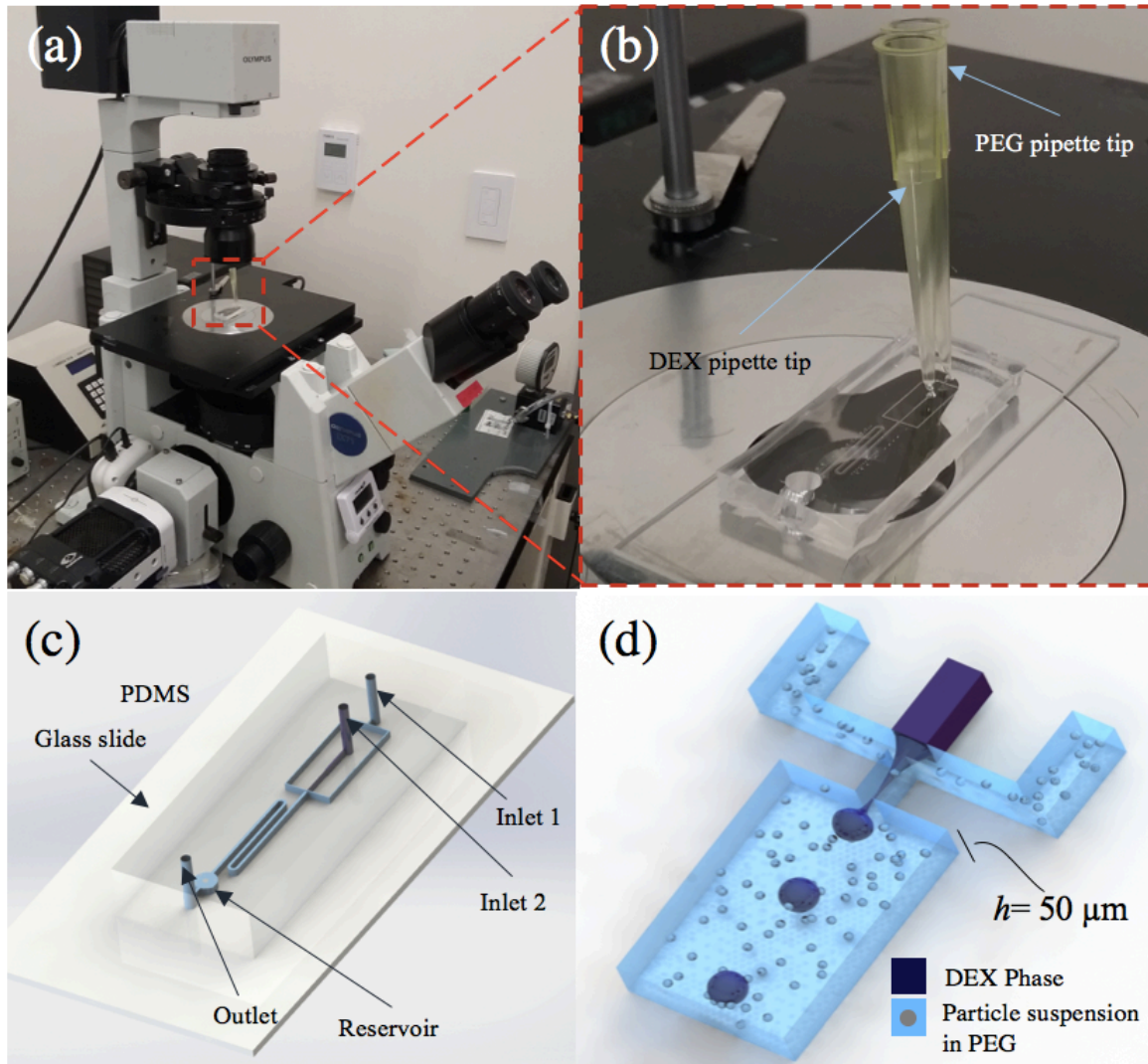


**Figure 4.** (a) An inverted microscope and a high-speed camera are used to monitor experiments and record videos. (b) Experimental setup of the microfluidic system, with pipette tips inserted at the inlets for infusion of the fluids into the chip. (c) Schematic diagram of the microfluidic device. A patterned PDMS slab is bonded to a glass slide, using a plasma chamber. (d) Schematic diagram of the flow-focusing junction of the microfluidic device. The droplets are generated at a flow-focusing junction with an orifice.

## 2.4 Results and discussion

Figure 5 shows time-series experimental images of particles partitioning to the interface of the DEX droplets, for different concentrations of  $d = 10 \mu\text{m}$  diameter carboxylated particles. Generally, it is observed that particle coverage on the DEX droplets increases with the amount of time the droplets spend in the serpentine microchannel, and higher particle concentrations result in more complete droplet coverage. The number of particles partitioning to the outer surface of the droplets is counted, for different particle sizes and different particle concentrations, from the moment the droplets are generated (which corresponds to time  $t = 0$  s) until they reach the reservoir ( $t \approx 450$  s). The degree of droplet coverage is defined as  $Nd^2/4D^2$ , as the ratio of  $N$ , the number of particles partitioned to the droplet, to  $4D^2/d^2$ , the maximum number of particles that the surface area of the droplet can geometrically accommodate. Here, it is assumed that each carboxylated particle, of diameter  $d$ , covers a surface area equal to  $\pi d^2/4$ .

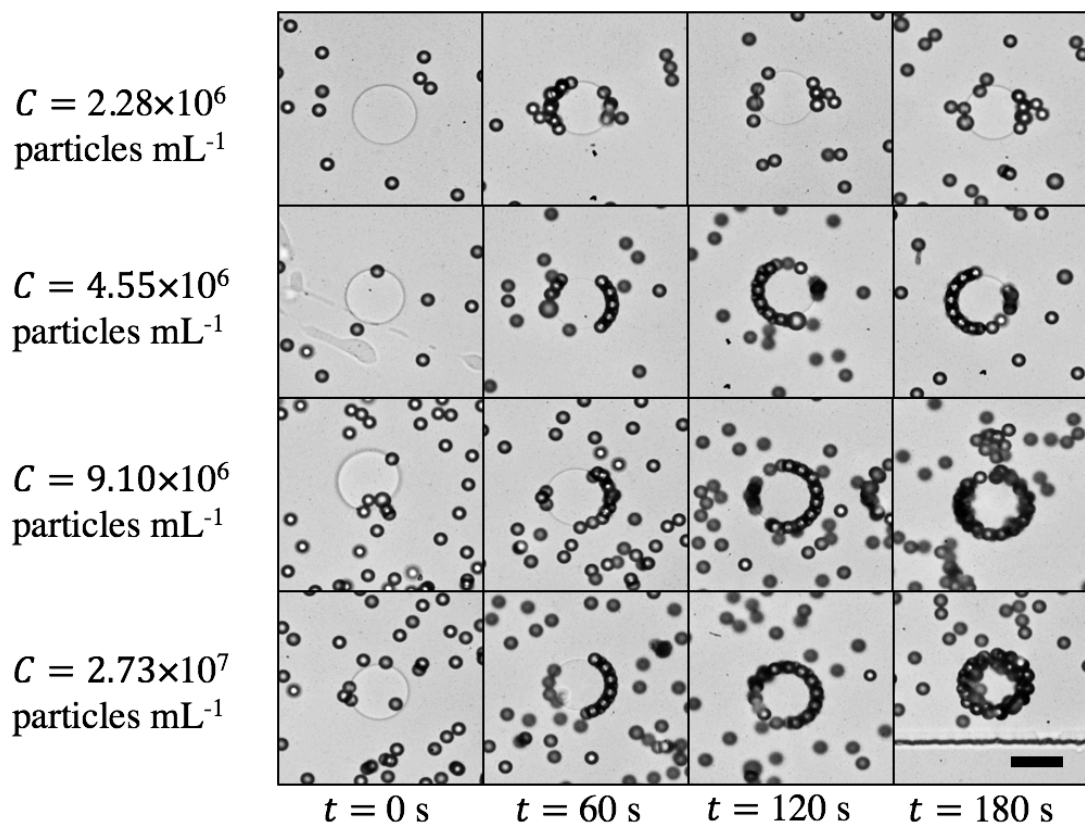


**Figure 5.** Time-series images of DEX droplets being covered with  $d = 10 \mu\text{m}$  diameter carboxylated particles, at different particle concentrations, in the serpentine region of the microfluidic device. Higher particle concentrations result in faster coverage of the DEX droplets. Scale bar indicates  $50 \mu\text{m}$ .

How well the carboxylated particles cover and remain on the interface of the DEX droplets is primarily affected by the competition between several physical phenomena. The binding energy or Gibbs desorption free energy  $\Delta G = \gamma d^2(1 - \cos\theta)^2/4$ ,<sup>91</sup> tends to keep the particles on the liquid-liquid interface. The polar interactions of water molecules across the interface of DEX and PEG affect the adsorption of the particle on the interface of the droplet. The Gibbs desorption free energy is opposed by energies that try to pull the particles away from the liquid-liquid interface, including the thermal energy  $kT$ , which is related to the random Brownian motion of carboxylated microparticles, the Stokes' drag-based shear energy on the particle  $6\pi\mu_{PEG}uD/2$ ,<sup>92</sup> and the electrostatic repulsion energy between the charged carboxylated particles and the liquid-liquid interface. Here,  $\theta$  is the contact angle between the liquid-liquid interface and the particle surface, Boltzmann's constant  $k = 1.38 \times 10^{-23} \text{ m}^2 \text{ kg s}^{-2} \text{ K}^{-1}$ , and temperature  $T = 293.15 \text{ K}$ . The droplet flow speed  $u = 6.1 \text{ } \mu\text{m s}^{-1}$  is kept constant in our experiments by careful tuning of the hydrostatic liquid column heights. The characteristic length used for defining the Stokes' drag-based shear energy is defined as the diameter of the DEX droplet,  $D$ . Specifically, the Stokes' drag based shear energy is defined here as the drag force exerted on a carboxylated particle on the interface of the DEX droplet as the droplet is traveling the distance  $D$ , at flow speed  $u$ .

It is known that an electrostatic repulsion energy exists between charged particles and oil-water interfaces, which affects the partitioning of charged particles onto the interfaces.<sup>72</sup> This electrostatic repulsion increases with the difference in the dielectric constants of the two phases that form the liquid-liquid interface.<sup>93</sup> However, in our experiments with water-in-water emulsions, the carboxylated particles do not experience significant electrostatic repulsion forces

from the liquid-liquid interface because the dielectric constants of both PEG and DEX phases, at such low polymer concentrations, are very close to that of water.<sup>94,95</sup> Therefore, electrostatic repulsion is neglected in the analysis.

To better understand how the remaining phenomena affect the ability of particles to remain on the liquid-liquid interface, the orders-of-magnitude of each energy are compared to one another. Keeping the particles on the interface is the Gibbs free energy of desorption  $\Delta G = O(10^{-18})$  J, where it is assumed that the two liquid phases have approximately the same degree of wetting on the particle surface, so the contact angle  $\theta = 90^\circ$ . The thermal energy  $kT = O(10^{-21})$  J, and the shear energy  $6\pi\mu_{PEG}udD/2 = O(10^{-18})$  J. Therefore, the thermal energy has a negligible effect on how well the carboxylated particles remain on the interface of the DEX droplets, and it is found that the competition between the binding and shear energies is what governs whether partitioned particles stay on the interface of the water-in-water droplets.

Using an order-of-magnitude estimation, by equating the two most dominant energies, the shear energy  $6\pi\mu_{PEG}udD/2$  and the binding energy  $\gamma d^2(1 - \cos\theta)^2/4$ , it is found that the critical carboxylated particle diameter  $d_c = O(1)$   $\mu\text{m}$ , below which carboxylated particles do not stay attached to the droplet interface. Carboxylated particles that are smaller than  $d_c = O(1)$   $\mu\text{m}$  experience a higher shear energy than the binding energy and as a result, can easily get washed away from the surface of the DEX droplets. On the other hand, particles that have diameters greater than  $d_c = O(1)$   $\mu\text{m}$  possess higher binding energy, compared to shear energy. Therefore, they stay on the surface of the DEX droplets.

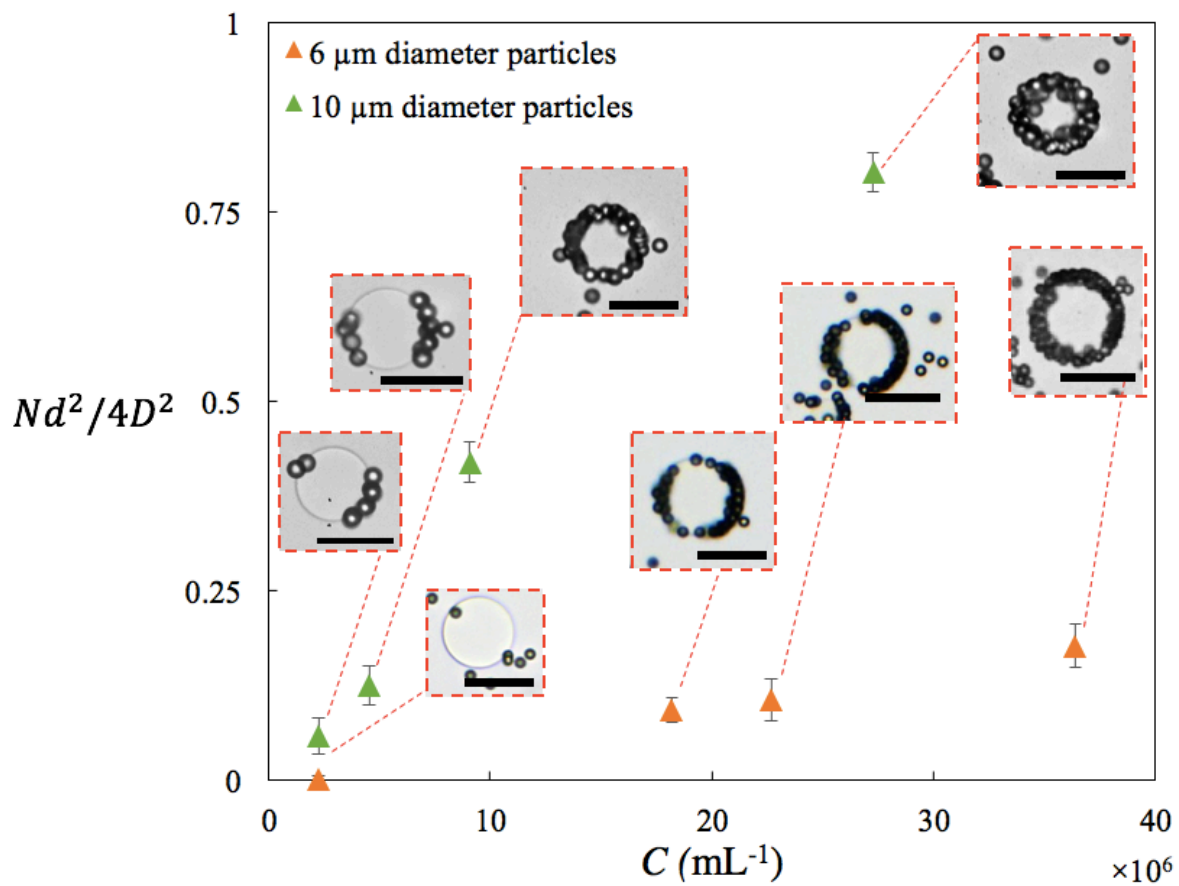
Figure 6 is a plot of the droplet coverage  $Nd^2/4D^2$  versus the particle number concentration  $C$ . Based on the results shown on Figure 6, particles of both diameters  $d = 10 \mu\text{m}$  and  $d = 6 \mu\text{m}$  stay on the surface of DEX droplets. This observation is consistent with the order-of-magnitude estimation of the critical particle diameter,  $d_c = O(1) \mu\text{m}$ , above which particles remain on the interface. It is found that droplet coverage increases monotonically with particle concentration for both particle sizes. As particle concentration increases, the chance of a particle colliding with the surface of the DEX droplets increases. The increase in particle-interface collisions increases the coverage of the DEX droplets.

Moreover, using larger  $d = 10 \mu\text{m}$  diameter particles results in better coverage, compared to stabilizing with the smaller  $d = 6 \mu\text{m}$  diameter particles. The lower DEX droplet coverage obtained with  $d = 6 \mu\text{m}$  diameter particles is an indication that this particle diameter is near the critical particle diameter  $d_c$ , below which shear stresses overcome the particle-interface binding energy, and particles detach from the droplet interface more easily.

Carboxylated particles with diameter  $d = 1 \mu\text{m}$  diameter with particle number concentration  $C = 4.55 \times 10^7$  particles  $\text{mL}^{-1}$  and  $C = 4.55 \times 10^8$  particles  $\text{mL}^{-1}$  are also used. These particles do not remain on the interface of the DEX droplets. Carboxylated particles that interact with the surface of the DEX droplets are washed away soon after, indicating that the shear energy on the particles is greater than the particles' binding energy to the DEX droplet interface. This observation further

demonstrates that the actual value of the critical carboxylated particle diameter,  $d_c$ , lies between 1 – 6  $\mu\text{m}$ .

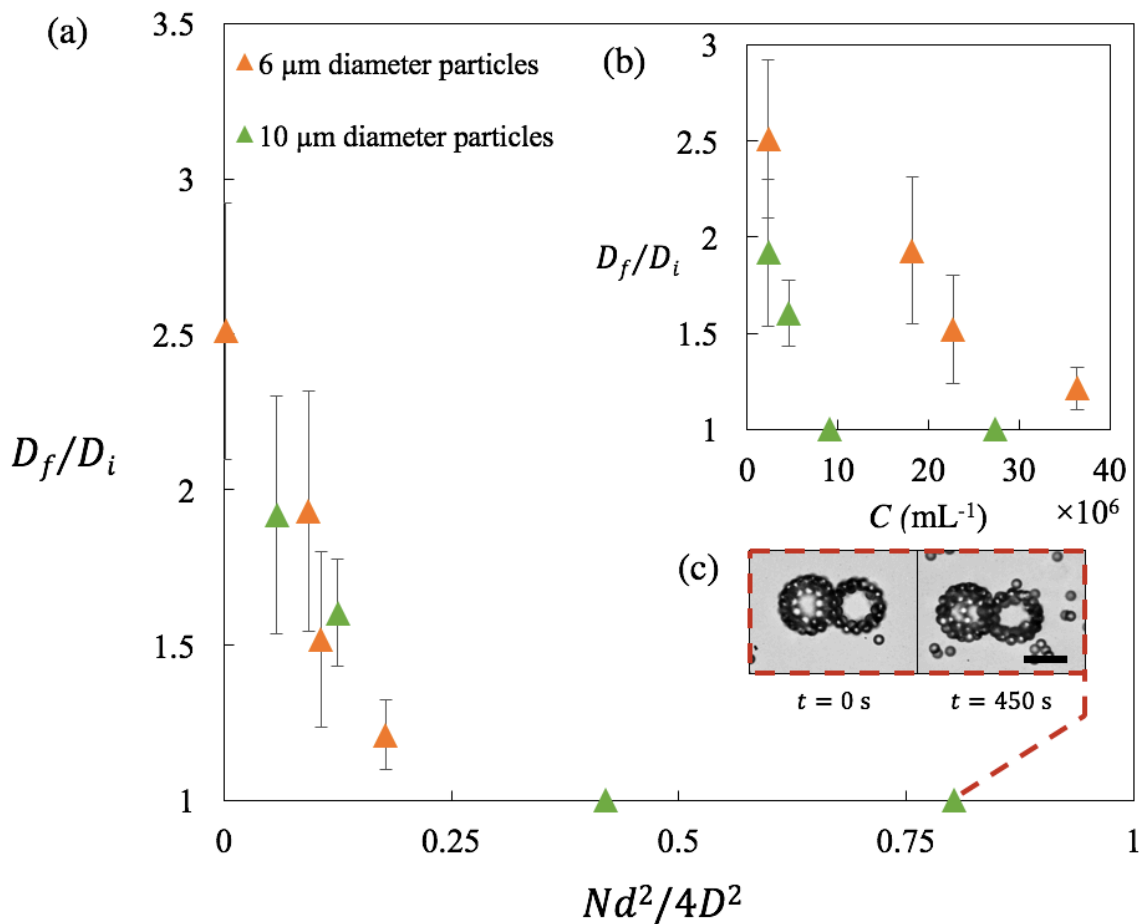
It is noted that in the current microfluidic geometry setup, the DEX droplets cannot achieve a complete droplet coverage  $Nd^2/4D^2 = 1$ , because the generated droplet diameter  $D$  is the same as the channel height  $h$ . Since the carboxylated particles cannot partition to areas of the droplet that are in contact with the PDMS (i.e. the top and bottom surfaces), a maximum droplet coverage  $Nd^2/4D^2 \approx 0.75$  is observed.



**Figure 6.** Plot of droplet coverage  $Nd^2/4D^2$  versus carboxylated particle number concentration  $C$  in the PEG phase. The coverage of the DEX droplets increases with the particle concentration and particle size. Scale bars indicate 50  $\mu\text{m}$ .

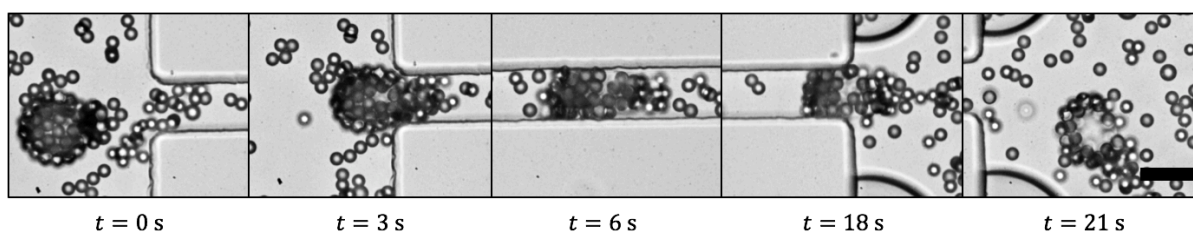
At the end of the microchannel, the DEX droplets flow into a large reservoir (see Figure 4), where the stability of particle-stabilized droplets against coalescence is quantified. As the DEX droplets enter the reservoir, they slow down and as a result, droplets come in contact with one another. To quantify the amount of coalescence taking place in the reservoir, the diameter of the DEX droplet entering the reservoir,  $D_i$ , is measured and compared with the diameter of the droplet exiting the reservoir  $D_f$ . The DEX droplets travel inside the reservoir for about  $t = 450$  s.

Figure 7(a) shows a plot of the diameter ratio,  $D_f/D_i$ , versus the coverage  $Nd^2/4D^2$ . As the coverage of the DEX droplets increases,  $D_f/D_i$  decreases, meaning that the droplets are becoming stable against coalescence and preserving their size. Figure 7(b) shows that for a given particle concentration, larger particle size results in lower incidences of coalescence.



**Figure 7.** (a) Plot of the final to initial droplet diameter ratio  $D_f/D_i$  versus droplet coverage  $Nd^2/4D^2$ . As expected, an increase in droplet coverage  $Nd^2/4D^2$  results in a decrease in the diameter ratio  $D_f/D_i$  indicating that droplets become stabilized against coalescence. (b) Plot of the final to initial droplet diameter  $D_f/D_i$  versus particle concentration  $C$ . (c) Inset shows a time-series of images of two particle-stabilized DEX droplets inside the reservoir of the microfluidic device. Despite being in contact over the course of 450 s, the two droplets do not coalesce. Scale bar indicates  $50 \mu\text{m}$ .

These particle-stabilized water-in-water emulsions also exhibit the ability to retain particle coverage under shear. Figure 8 shows a time-series of images of a single particle-stabilized emulsion squeezing through a small microchannel construction, inside the reservoir of the microfluidic device. Despite the low free energy of desorption of the particles, only a small number of particles desorb from the DEX droplet surface while the droplet squeezes through the constriction. The particle aggregation observed in Figure 8 can be attributed to the binding energy between the particles, as a result of the presence of PEG molecules inside the particle suspension.<sup>96</sup>



**Figure 8.** Time-series images of a particle-stabilized DEX droplet squeezing and flowing through a narrow constriction, which is located inside the reservoir of the microfluidic device. Stabilizing particles have diameter  $d = 10 \mu\text{m}$ . Most particles remain on the droplet as the droplet exits the narrow constriction and return to a spherical shape. The scale bar indicates  $50 \mu\text{m}$ .

As a proof-of-concept example of the biotechnological application of this system, AML cells are encapsulated using this platform, in a water-in-water DEX droplet that is stabilized by  $d = 10 \mu\text{m}$  diameter carboxylated particles. Figure 9 shows the encapsulation of an AML cell inside a particle-stabilized DEX droplet. The biocompatibility of these APTS-based particle-stabilized emulsions make them a good alternative to water-in-oil emulsions for cell-encapsulation and immunoisolation purposes, and other biotechnological applications. Based on our AML cells

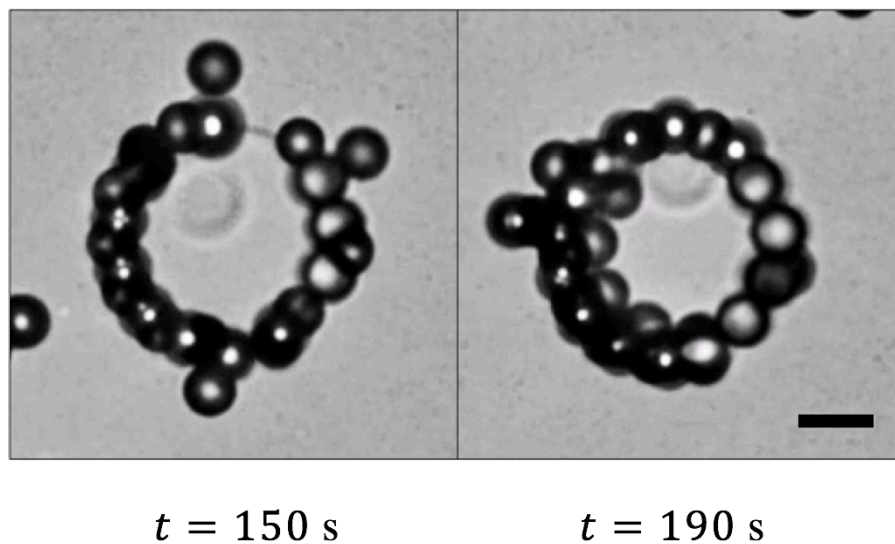


**Figure 9.** Time series images of a single particle-stabilized DEX droplet encapsulating an AML cell. The particles are 10  $\mu\text{m}$  in diameter. Scale bar indicates 20  $\mu\text{m}$ .

viability studies (see Figure 10), the presence of DEX does not impinge on the viability of the AML cells.

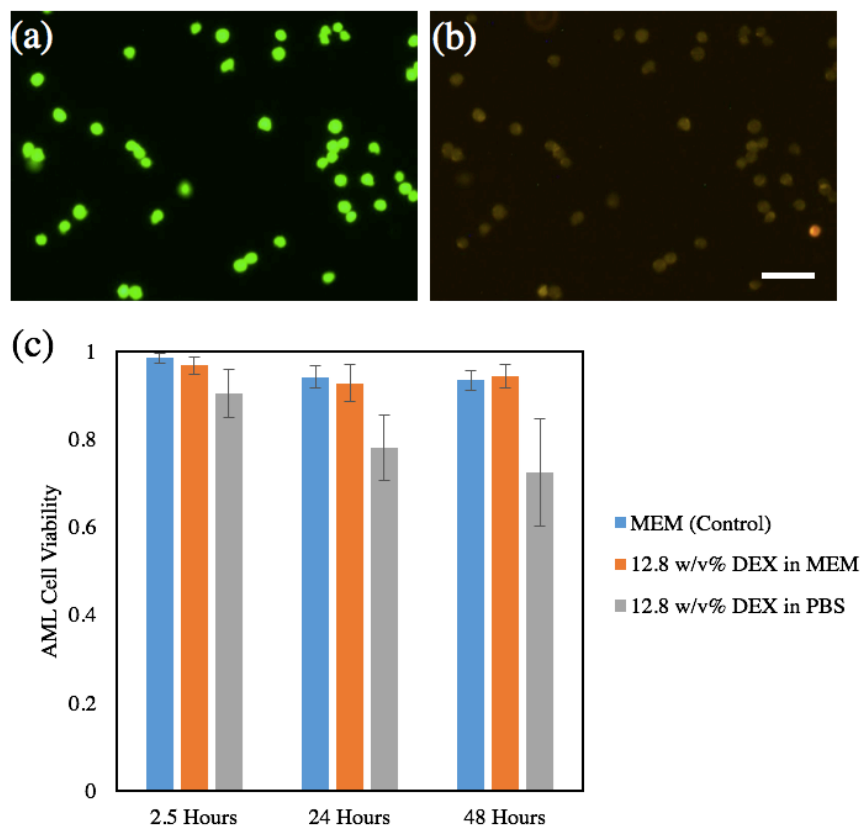


**Figure 10.** Fluorescence images of (a) live and (b) dead cells stained with calcein AM (green) and ethidium homodimer-1 (red), respectively. (c) The addition of DEX to a suspension of cells in MEM does not reduce the viability of the AML cells. The lack of nutrients in the solution of 12.8 w/v% DEX in PBS may be the cause of the lower AML cells viability observed in (c). Scale bar indicates 50  $\mu\text{m}$ .

## 2.5 Conclusions

In this chapter, a microfluidic platform is presented that enables the generation and stabilization of water-in-water emulsions, using carboxylated particles. A flow-focusing microfluidic device is used to generate water-in-water emulsions of DEX-in-PEG. Carboxylated particles that are suspended in the continuous phase of PEG gradually partition to the outer surface of DEX droplets, and over time, they cover the droplets. Changes in the particle size and the particle concentration affect the coverage and stability of the DEX droplets. Owing to their intrinsic biocompatibility, particle-stabilized water-in-water emulsions are a good alternative for traditional particle-stabilized water-in-oil emulsions. These emulsions could be utilized in a variety of biotechnological applications, such as cell encapsulation and drug delivery.

# Chapter 3

## Spiky microparticle generation by integrating ionic cross-linking within an aqueous two-phase system

The work presented in this chapter is based on a manuscript, which is in preparation for submission to a peer reviewed journal *Nature Materials*.

Abbasi, N., Navi, M., Tsai, S. S. H. (2018). Spiky microparticle generation by integrating ionic cross-linking within an aqueous two-phase system

### 3.1 Abstract

Non-spherical microparticles have shown to be more effective, compared to round microparticles, at controlled release or adsorption of different macromolecules. Therefore, generating nonspherical particles, which possess a high surface area to volume ratio, is highly desirable. Herein, a new method of generating spiky microparticles, based on the ionic cross-linking of alginate and calcium chloride ( $\text{CaCl}_2$ ) within an aqueous two-phase system (ATPS) of dextran

(DEX) and polyethylene glycol (PEG), is presented. First, a thread of DEX-alginate is formed, surrounded by a dispersed phase of PEG, inside a flow-focusing microfluidic device. The thread of DEX-alginate breaks up into droplets, due to Rayleigh-Plateau instability, inside the outlet tubing of the microfluidic device. The emulsions then flow into a bath of PEG and  $\text{CaCl}_2$ . The PEG that flows into the bath with the droplets delays the polymerization of the DEX-alginate droplets by slowly allowing the calcium chloride to diffuse through. As the emulsions flow into the bath, which contains the PEG with calcium chloride, the emulsion system goes out of chemical equilibrium. To reach a new chemical equilibrium, water molecules from the DEX-alginate droplets start to diffuse out slowly, and combined with gelation due to the presence of calcium chloride in the surrounding phase, form spikes. The slow diffusion of calcium chloride towards the droplets triggers the polymerization of the droplets. Over time, polymerized spiky microparticles are generated inside the PEG-calcium chloride bath. It is observed that the length of the spikes across the microparticles can be tuned by varying the concentration of PEG in the bath ( $C_{PEG}$ ). As we increase the concentration of the PEG inside the bath, the final length of spikes decreases. These spiky microparticles may find use in different biotechnological applications, for example, as drug delivery vehicles.

## 3.2 Introduction

Microparticles have been utilized in a variety of different fields, such as in the development of biomaterials for drug delivery applications. The encapsulation of drugs within polymeric microparticles is desirable because therapeutic agents can be sustained and protected inside the

microparticles for a long time, before their release, which in turn ensures a reduction in the amount of drug needed.<sup>97-99</sup>

The design of microparticles as drug delivery vehicles involves considering different design parameters. Chemical properties of microparticles, and their effects on degradation,<sup>100</sup> as well as the surface chemistry of the microparticles and the resulting interaction with targeted cells and tissues have been studied extensively.<sup>101,102</sup> Material selection for the microparticles is essential, since it not only affects the particles' biodegradability and the uptake mechanism, it also limits the types of therapeutic drugs which can be encapsulated within the microparticles.<sup>103</sup> The materials used for generating microparticles include polylactic acid (PLA),<sup>104-107</sup> polyglycolic acid (PGA),<sup>108</sup> copolymers of PLA and PGA (PLGA),<sup>109,110</sup> PEG,<sup>111</sup> polyethylene oxide (PEO),<sup>112,113</sup> and DEX.<sup>114-116</sup>

Besides chemical properties, the physical properties of microparticles, such as microparticle size, impact the functionality and performance of these particles as delivery vehicles. The size of the microparticles influences the degradation of the carrier,<sup>117</sup> and moreover, it affects the diffusion of the vehicles in blood vessels and airways, ultimately, impacting the adhesion of the microparticles to targeted tissues.<sup>118,119</sup>

One physical design parameter, which has not been explored much in the literature, is the delivery vehicles' shape.<sup>99</sup> In nature, there are plenty of examples of particles where function and performance rely heavily on their shape, such as with spiky pollen grains.<sup>120</sup> Recent studies in the

literature have shown that non-spherical microparticles are more beneficial, compared to their spherical counterparts, for drug delivery purposes.<sup>121</sup> Specifically, the high surface area to volume ratio of non-spherical microparticles allows for better attachment, and also changes the internalization of the microparticles into the targeted cells and tissues.<sup>99,119</sup>

Researchers have developed a variety of different methods for generating non-spherical microparticles for drug delivery purposes. These techniques utilize droplet microfluidics,<sup>122–124</sup> photopolymerization,<sup>125–127</sup> lithography integrated within microfluidics,<sup>128–131</sup> and electrospray.<sup>132,133</sup> The challenges associated with generating more complex non-spherical microparticles has motivated some researchers to utilize natural microparticles as delivery vehicles. One such natural microparticle is pollen grains.<sup>120</sup> The spikes across the surface of pollen grains provide a much higher surface area to volume ratio, compared to other synthetic non-spherical microparticles.

Although pollen grains are promising for drug delivery applications, post-processing steps required to extract the pollen grains are cumbersome, requiring harsh chemical processing.<sup>120,134,135</sup> Furthermore, loading drugs into pollen grain microparticles,<sup>120</sup> and functionalizing the surface of these microparticles is challenging,<sup>136</sup> Manipulating physical features of natural pollen grains, such as spike length and particle diameter core, is not possible. Given the tremendous physical attributes of pollen microparticles, and their spike features, it is desirable to be able to generate synthetic microparticles with spikes across their surface, whose spike lengths could be tuned and furthermore, be easily functionalized with different reagents. Current techniques of generating

pollen-like microparticles involve utilizing natural pollens as templates, through sol-gel coating,<sup>137,138</sup> which limits tuning of different chemical and physical characteristics of the microparticles.

In this chapter, inspired by the spiky morphology of pollen micrograins, a novel and facile technique for generating pollen-like spiky microparticles is presented. Here, all-biocompatible spiky microparticles are generated through ionic cross-linking of alginate and  $\text{CaCl}_2$ , within an ATPS of DEX and PEG. Droplets of DEX-alginate, surrounded by PEG, are formed within a microfluidic device. To trigger the polymerization, spike growth across the DEX-alginate droplets, the emulsions are flowed into a polymerization bath of PEG- $\text{CaCl}_2$ . Spikes form across the DEX-alginate droplets due to the sudden instability caused across the DEX-PEG interface. Over time, the spikes grow, until all of the alginate from the droplet phase cross-link with the  $\text{CaCl}_2$  in the PEG- $\text{CaCl}_2$  bath, halting the spike growth. The effects of changes in the polymerization bath's  $C_{PEG}$ , and  $\text{CaCl}_2$  concentration, on the spike growth, are explored independently from one another. It is shown that the length of the spikes across the DEX-alginate droplets can be tuned by varying the concentration of the PEG inside the polymerization bath.

## 3.3 Experimental methods

### 3.3.1 Chemical preparations

To ensure that the ATPS is in equilibrium, alginate needs to be premixed with DEX and PEG phases, before phase separation. Furthermore, the concentrations of the PEG and DEX phases need

to be chosen such that alginate partitions mostly to the droplet phase, in this case, the DEX phase. To find the most optimal concentration of DEX and PEG, three different ATPSs are made. All three ATPSs are prepared with PEG 10 w/v% stock solution (PEG;  $M_w$  35k, Sigma Aldrich, St. Louis, MO, USA), while the DEX concentration is varied from 10 w/v% to 30 w/v% (DEX,  $M_w$  500k, Pharmacosmos, Holbaek, Denmark). Equal volumes of the DEX and PEG stock solutions are made for each system, in deionized (DI) water, and mixed inside a Falcon<sup>TM</sup> tube (BD Medical, Franklin Lakes, NJ, USA). Subsequently, 1 w/v% alginate (Alginic acid sodium salt, Sigma Aldrich, St. Louis, MO, USA) is added to each ATPS, and left to phase separate for 48 hours. After phase separation, the top phase (equilibrated PEG phase) and the bottom phase (equilibrated DEX phase) are separated and transferred to separate Falcon<sup>TM</sup> tubes for each ATPS. It is observed that as the DEX concentration increases (given fixed PEG concentration of 10 w/v%), the amount of alginate partitioning to the DEX phase increases. Therefore, the ATPS of PEG 10 w/v% and DEX 30 w/v% is chosen for droplet generation.

A mixture of PEG stock solution (PEG;  $M_w$  35k, Sigma Aldrich, St. Louis, MO, USA) and  $\text{CaCl}_2$  ( $\text{CaCl}_2$  dihydrate, Sigma Aldrich, St. Louis, MO, USA) is used in the polymerization bath. To study the effect of changes in  $C_{PEG}$  on spike growth, stock solutions of PEG 10, 15, 20 and 30 w/v%, each with 2 w/v%  $\text{CaCl}_2$ , are prepared in DI water. Moreover, stock solutions of PEG 10 w/v% with 2, 8, 10 and 20 w/v%  $\text{CaCl}_2$  are prepared to explore the effects of changes in  $\text{CaCl}_2$  concentration on the spike growth.

### 3.3.2 Device fabrication

Standard soft lithography technique is used to fabricate the flow-focusing microfluidic device.<sup>3</sup> The flow-focusing microfluidic design, with two inlets and one outlet, is drawn on a computer-aided design (CAD) software (AutoCAD 2016, Autodesk, Inc., San Rafael, CA, USA). Then, this design is used to print a patterned photomask, on a transparency sheet (CAD/ART Services Inc., Bandon, OR, USA).

To generate the microfluidic channel mold, SU-8 2050 photoresist (Microchem, Newton, MA, USA) is spin coated on a 4-inch diameter silicon wafer (UniversityWafer, Inc., Boston, MA, USA) and subsequently exposed to UV light through the patterned photomask. The patterns are developed by immersing the wafer inside developer solution (UniversityWafer, Inc., Boston, MA, USA).

Once the mold is ready, it is filled with a 10:1 ratio mixture of polydimethylsiloxane (PDMS) resin and curing agent (Sylgard 184, Dow Corning, Midland, MI, USA). The mixture of the PDMS resin and curing agent inside the mold is left in a 70° oven, for an hour. Once the mixture cures, the PDMS slabs are cut out from the mold. A 1 mm diameter biopsy punch is used for making two inlets, and one outlet. Finally, the PDMS slab is bonded to a glass slide, through oxygen plasma treatment (Harrick Plasma, Ithaca, NY, USA).

### 3.3.3 Experimental setup

The experiments are monitored through an inverted microscope (AX10, Carl Zeiss AG, Oberkochen, Germany), and a high-speed camera (Miro M110, Vision Research, Wayne, NJ, USA). To process experimental images, the ImageJ<sup>TM</sup> software is used.

Syringe pumps (Harvard Apparatus, Holliston, MA, USA) are used to flow the dispersed phase of DEX-alginate, and the continuous phase of PEG, into the flow-focusing microfluidic device, through tubings (1/32" ID 3/32" OD Tygon Tubing, Saint-Gobain, Malvern, PA, USA). The dispersed phase of DEX-alginate flows at a flow rate of  $1 \mu\text{l min}^{-1}$ , and the continuous phase of PEG is pumped at a flow rate of  $20 \mu\text{l min}^{-1}$ . Due to the low interfacial tension of the ATPS, a long thread of DEX-alginate is formed, surrounded by the PEG phase inside the microfluidic device. The thread breaks off, due to the Rayleigh-Plateau instability of the ATPS,<sup>79</sup> inside the tubing connected to the outlet; forming droplets of DEX-alginate in the continuous phase of PEG. We observe that the diameter of the DEX-alginate droplets,  $d$ , ranges from 50-80  $\mu\text{m}$ .

As seen in Figure 11, the emulsions formed inside the outlet tubing flow into a polymerization bath (60mm  $\times$  15mm polystyrene petri dish, Fisher Scientific, NH, USA) filled with PEG-CaCl<sub>2</sub> solution for 30 s. Then, the outlet tubing is removed from the polymerization bath, and the DEX-alginate droplets, in a bulb of PEG (intermediate PEG phase), are observed in the solution of PEG-CaCl<sub>2</sub> (outer PEG phase), as they grow spikes over time.

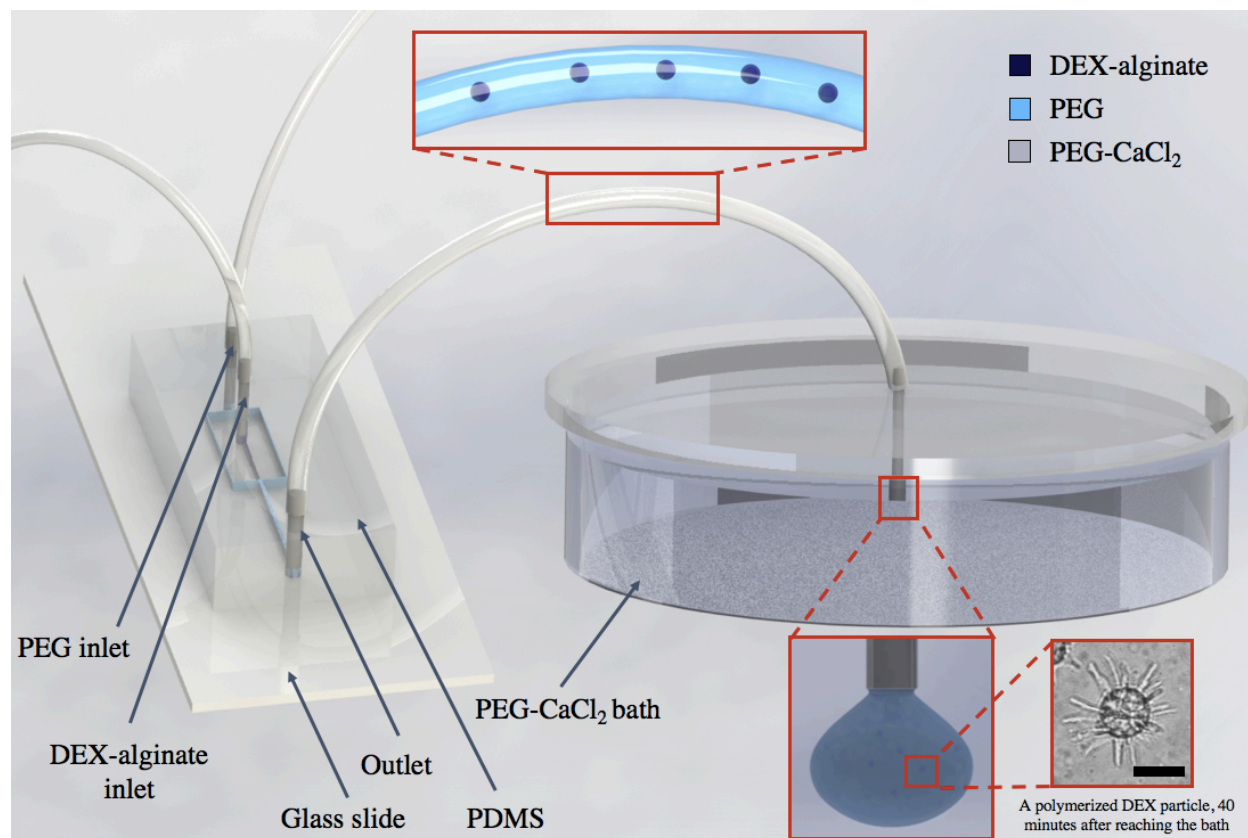


**Figure 11.** Schematic diagram of the experimental setup. A flow-focusing microfluidic device is used to generate emulsions of DEX-alginate in the continuous phase of PEG. The DEX-alginate droplets, which are generated inside the outlet tubing, flow into a bath of PEG-CaCl<sub>2</sub> solution, for 30 s. Then, the flows of DEX-alginate and PEG are stopped, the outlet tubing is disconnected from the PEG-CaCl<sub>2</sub> bath, and the bath of PEG-CaCl<sub>2</sub> is placed on an inverted microscope, to observe the polymerization and growth of spikes across the DEX-alginate droplets over time. The scale bar indicates 50  $\mu\text{m}$ .

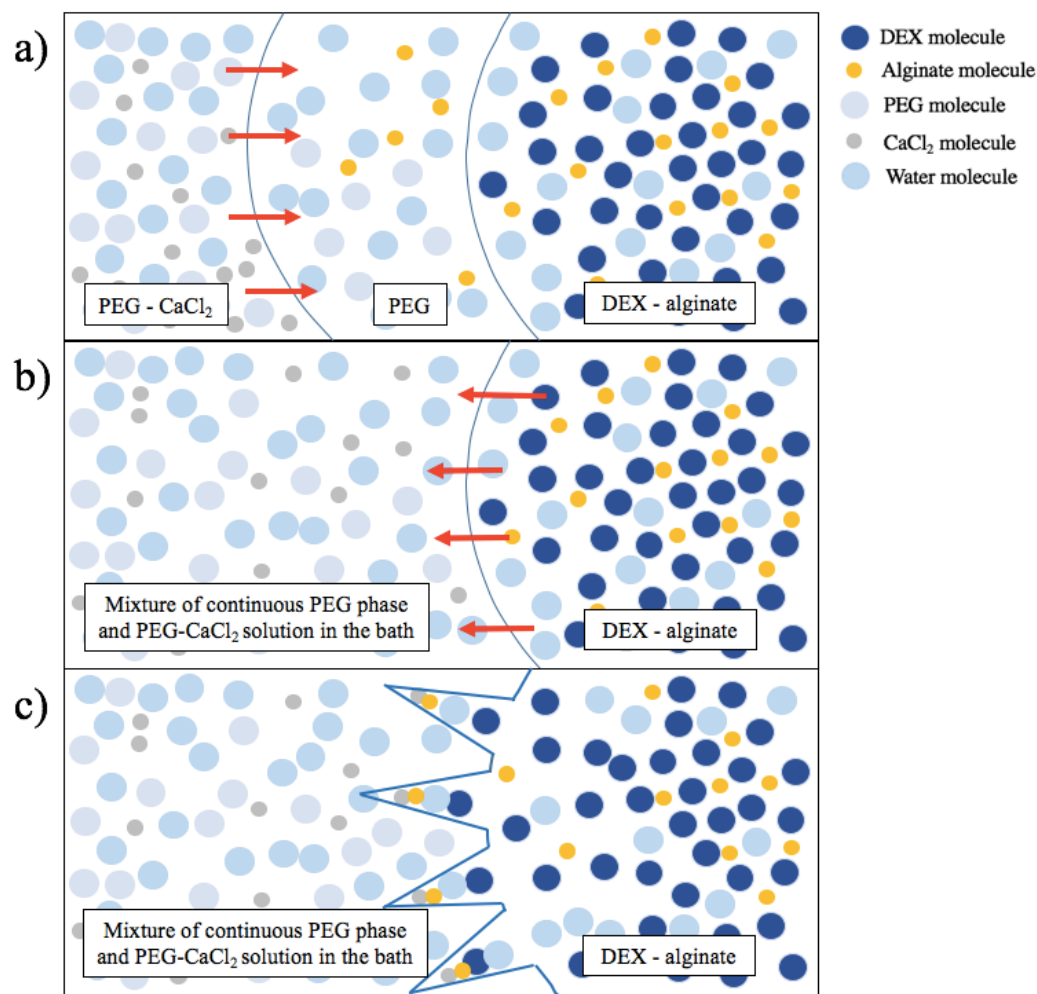
### 3.4 Results and discussion

The process of spike formation on the DEX-alginate droplets is governed mainly by a combination of diffusion, electrostatic transport, and the simultaneous ionic cross-linking of alginate and calcium ions (as shown in Figure 12). The DEX-alginate droplets, surrounded by PEG, flow into the bath of PEG-CaCl<sub>2</sub>. A small bulb of PEG (intermediate PEG phase), containing the DEX-alginate droplets, forms inside the PEG-CaCl<sub>2</sub> bath (outer PEG phase). The concentration gradient between the outer PEG phase and intermediate PEG phase drives the water and CaCl<sub>2</sub> molecules across the two PEG phases.

As the PEG solution in the bulb, and the PEG-CaCl<sub>2</sub> form a homogenous mixture, the DEX-alginate droplets go out of chemical equilibrium with their surrounding phase. To reach a new chemical equilibrium, water molecules from the DEX-alginate droplets leave the droplets, in the form of fingers. Simultaneously, as the water molecules from the DEX-alginate droplet are leaving the droplet core, the fingers come in contact with the surrounding homogeneous mixture of PEG-CaCl<sub>2</sub>. The presence of CaCl<sub>2</sub> around the DEX-alginate droplets triggers ionic polymerization between carbonate ions from the alginate, and the calcium ions from CaCl<sub>2</sub>. This, in turn, hinders growth of the fingers and overtime, results in the termination of growth and allows for the generation of polymerized spiky microparticles.

Interestingly, it is found that the growth of the spikes across DEX-alginate droplets is highly dependent on the presence of alginate molecules in the DEX-alginate droplets' surrounding continuous PEG phase. The ATPS of DEX and PEG, with alginate only added after phase

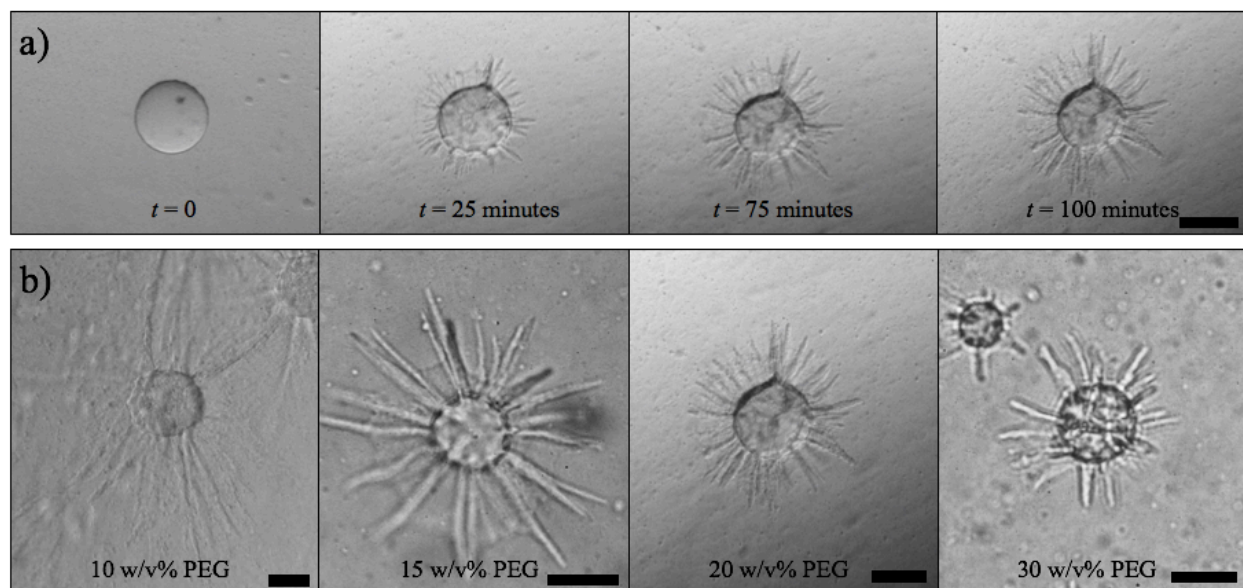
separation to the DEX phase, in the dispersed phase, does not produce spikes across the DEX droplets, nor do the droplets become polymerized (even after monitoring them for 24 hours). This is an indication that the presence of the alginate not only in the droplet phase, but also in the dispersed phase of PEG, is crucial for the spike growth across droplets, and their subsequent polymerization. This can be explained by the electrostatic interactions between the alginate molecules present in the intermediate PEG phase, and the  $\text{CaCl}_2$  molecules present in the outer PEG phase. This electrostatic interaction draws the  $\text{CaCl}_2$  molecules towards the intermediate PEG phase, triggering the polymerization with simultaneous instability across the DEX-alginate droplets.



**Figure 12.** Process of spike formation across a DEX-alginate droplet. a) The DEX-alginate droplet reaches the polymerization bath of PEG- $\text{CaCl}_2$ . Water molecules diffuse between the PEG- $\text{CaCl}_2$  solution, and the intermediate PEG phase, resulting in a homogeneous mixture. b) The DEX-alginate droplet goes out of equilibrium with its surrounding, so to reach a new equilibrium, water molecules from the DEX-alginate droplet migrate outside. c) Water molecules flow out from the DEX-alginate droplets in the form of fingers. The simultaneous ionic cross linking of alginate in the droplets and fingers, and the  $\text{CaCl}_2$  in the surrounding PEG phase results in polymerization of the spiky DEX-alginate particles.

Figure 13(a) represents time-series images of a DEX-alginate droplet inside the polymerization bath of 20 w/v% PEG – 2 w/v% CaCl<sub>2</sub>. Time  $t = 0$  represents the time at which the flow of the emulsions to the bath is stopped. The spikes start to grow across the DEX droplet's surface, with the highest growth rate at the beginning. With time, the growth rate decreases, until the spike growth terminates. Spike growth across DEX-alginate droplets in the polymerization bath of 20 w/v% PEG – 2 w/v% CaCl<sub>2</sub> terminates at  $t = 100$  minutes.

Two different parameters are tuned, independently from one another, to explore the spike growth across the DEX-alginate droplets:  $C_{PEG}$ , and the concentration of the CaCl<sub>2</sub> in the polymerization bath. The final length of the spikes on the DEX-alginate particles can be tuned by varying only the concentration of the PEG used in the PEG-CaCl<sub>2</sub> solution inside the bath, whereas the CaCl<sub>2</sub> concentration does not have any impact on the spike growth. As seen in Figure 12(b), the increase in  $C_{PEG}$  from 10 w/v% to 30 w/v%, while keeping the CaCl<sub>2</sub> concentration at 2 w/v%, results in shorter final spike lengths. This can be explained by considering the diffusion of CaCl<sub>2</sub> molecules within the polymerization bath. The concentration gradient between the PEG-CaCl<sub>2</sub> solution in the bath and the intermediate PEG phase increases with the increase of  $C_{PEG}$ , from 10 w/v% to 30 w/v%. This higher concentration gradient results in a greater flux of CaCl<sub>2</sub> molecules migrating towards to the DEX-alginate droplets. Therefore, the spike growth gets halted at a faster rate, as a result of ionic crosslinking of alginate and calcium ions.



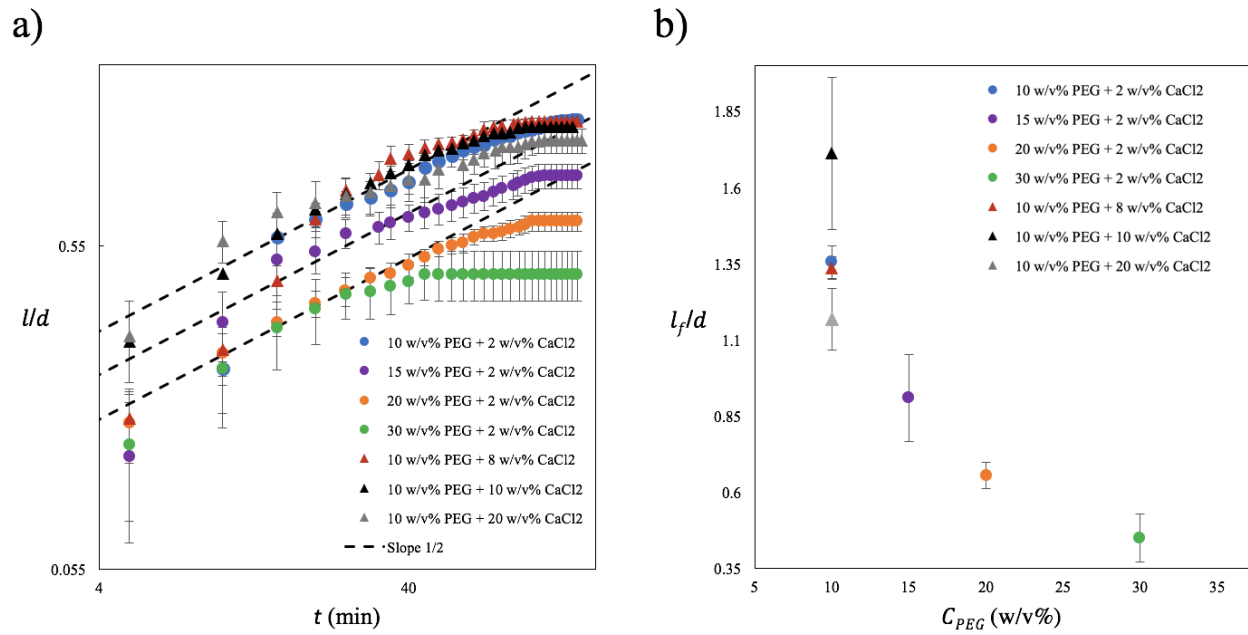
**Figure 13.** (a) Time-series images of a 30 w/v% DEX - 1 w/v% alginate droplet inside a bath of 20 w/v% PEG - 2 w/v%  $\text{CaCl}_2$ . With increasing time, the droplet starts to polymerize, spikes form over its surface and grow until the spike growth reaches a stable length at time  $t = 100$  minutes. (b) The final-state images of DEX-alginate particles, in different polymerization baths. With a fixed 2 w/v%  $\text{CaCl}_2$  concentration, the final spike length of particles decreases with increasing  $C_{PEG}$  inside the bath. Scale bars indicate 50  $\mu\text{m}$ .

Figure 14(a) shows the log-log plot of the normalized spike length  $l/d$  (where  $l$  is the spike length) versus time  $t$ , for different polymerization bath compositions. The spike formation across the DEX-alginate droplets starts off with a high growth rate and with time, the growth rate decreases, until it reaches a plateau. The increase in  $C_{PEG}$  from 10 w/v% to 30 w/v%, while keeping the  $CaCl_2$  concentration constant at 2 w/v% (Figure 14 (a), solid circle data points), results in a decrease of spike growth rate and, produces particles with shorter spikes. The longest spikes ( $l/d \approx 1.7$ ) produced formed in a polymerization bath of 10 w/v% PEG - 2w/v%  $CaCl_2$ , and the shortest spikes ( $l/d \approx 0.45$ ) are produced in the most viscous polymerization bath, containing 30 w/v% PEG – 2w/v%  $CaCl_2$ .

From Fick's second law of diffusion it is found that  $l \approx \sqrt{Dt}$ , where  $l$  is the diffusion length (in this case the spike length) and  $D$  is the diffusion coefficient, therefore,  $l \sim t^{1/2}$ .<sup>13</sup> The data series presented in Figure 14(a), at early times, follow a line indicated by a slope of  $1/2$ , which is evidence that diffusion likely governs spike growth generation across the DEX-alginate droplets at early stages. Another observation is that the final length of spikes decreases with increasing  $C_{PEG}$  in the PEG –  $CaCl_2$  bath. Here, as the concentration of the PEG inside the PEG -  $CaCl_2$  increases, the viscosity of the PEG- $CaCl_2$  in the bath increases. The increase in the PEG -  $CaCl_2$  viscosity results in a decrease of the diffusion coefficient  $D$ ,<sup>139</sup> which can in turn affect the spike lengths and result in the generation of shorter spikes.

Quantitatively, it is observed that increasing the  $CaCl_2$  concentration from 2 w/v% to 20 w/v%, while maintaining the  $C_{PEG} = 10$  w/v%, does not significantly affect the spike growth rate, and

the final spike length. Therefore, the primary parameter affecting the spike growth appears to be the concentration of the PEG in the bath,  $C_{PEG}$ . Figure 14(b) illustrates that the normalized final length of spikes  $l_f/d$ , decreases with  $C_{PEG}$ . As  $C_{PEG}$  increases from 10 to 30 w/v%, the normalized final length of spikes  $l_f/d$  drops from 1.7 to 0.45.



**Figure 14.** (a) Log–log plot of the normalized spike length  $l/d$  versus time  $t$ , for different polymerization bath compositions. Given fixed CaCl<sub>2</sub> concentration in the bath, as  $C_{PEG}$  increases, the final length of spikes observed across the DEX-alginate particles decreases. Further, the spikes’ growth across the DEX-alginate particles reaches a plateau faster when surrounded by a more concentrated PEG in the bath. (b) Plot of normalized final spike length  $l_f/d$  versus PEG concentration in the polymerization bath  $C_{PEG}$ . The final spike length  $l_f/d$  decreases with the concentration of the PEG solution inside the bath.

## 3.5 Conclusions

In conclusion, a new and facile method of generating non-spherical microparticles, with a high surface area to volume ratio, is presented. This method is unique in that it does not require complex syntheses or manipulation, yet generates highly controllable, and biocompatible, spiky microparticles. Using ATRP, integrated with ionic cross-linking allows for the generation of all-biocompatible pollen-like microparticles, without the need of additional post processing. It is shown that the length of the spikes can be tuned by changing the concentration of the PEG polymer present in the polymerization bath. Furthermore, this particle synthesis technique can be used and implemented for generating spiky surfaces, and spiky threads, which may find various biotechnological applications.

# Chapter 4

## Concluding remarks

In this thesis, the great potential of ATPS for the development of lab-on-a-chip systems and biomaterials is explored. Particle-stabilized emulsions of DEX-in-PEG are shown to be generated within a microfluidic platform, which could eventually be used for immunoisolation purposes, and spiky microparticles are formed through ionic cross-linking of alginate and calcium chloride, within an ATPS of PEG and DEX, which could be used for drug delivery purposes.

ATPS allows for the development of all-biocompatible microfluidic platforms, thereby removing the need for additional post processing washing steps. Utilizing the affinity partitioning capability of these systems, and careful selection of samples and reagents (such as selection of carboxylated particles as stabilizing agents), allows for the development of functional lab-on-a-chip systems. Moreover, manipulating the chemical equilibrium conditions of these systems, while integrating other chemical reactions, can lead to the generation of novel materials (such as the spiky microparticles).

Although it is shown that particle-stabilized water-in-water emulsions formed are capable of immunoisolation purposes, some improvements are still necessary to make the particle-stabilized emulsion system more functional. Integrating a microneedle and utilizing a 3D flow-focusing microfluidic device allows for generation of droplets that are smaller than the channel height.<sup>140</sup> In the current microfluidic setup, the diameter of droplets which are generated is the same as channel height. Therefore, the top and bottom of the droplets touch the walls of the microchannel, and as a result, particles cannot cover those areas. Using a needle device, it would then be possible to generate particle-stabilized droplets that have a 100% coverage since the droplets smaller than the channel height can be formed.

Moreover, once fully-stabilized emulsions are formed, it is possible to remove the core of the droplet phase, by introducing an extremely concentrated continuous phase. To reach a new chemical equilibrium, water molecules would leave the droplet phase, which in turns results in the generation of a hollow microcapsule, similar to hollow colloidosomes formed by water-in-oil systems.<sup>60,141</sup>

For the spiky microparticles, future work may involve integrating release of an encapsulated drug within the DEX droplet core, and analyzing the release profile. Moreover, in depth analysis of the process which governs the spike formation is required. This can be pursued by integrating mathematical modeling, and studying whether or not the experimental data for the spike lengths at different experiments, follow the mathematical model. Moreover, using the same chemicals can

lead to the generation of textured surfaces, and spiky threads, which may have application in biotechnology.

ATPSs possess a great potential. The biocompatible nature of these systems makes them a great alternative to conventional water-in-oil droplet microfluidic platforms. As researchers have overcome the challenges associated with generating water-in-water emulsions, the future works of ATPSs within microfluidic platforms will involve creating systems, and exploiting the affinity partitioning of different chemicals within each phase to make platforms functional. For instance, integrating other aqueous solutions, such as cell growth media, within the droplet phase of an ATPS microfluidic emulsion system allows for generation of more viable cell encapsulation vehicles, where the cells would be able to receive their nutrients. Moreover, expanding these systems from two to three distinct phases, such as a combination of DEX, Ficoll, and PEG,<sup>54</sup> and utilizing the affinity partitioning of each of the phases microfluidic platforms, can lead to generation of more complex, such as synthetic cells.

# Appendix

## A1. Order-of-Magnitude Approximations

The order-of-magnitude approximation calculation can be found below for the Gibbs desorption free energy, thermal energy, and Stokes' drag-based shear energy below.

### Gibbs desorption free energy

The Gibbs desorption free energy can be found by the following:

$$\Delta G = \gamma d^2 (1 - \cos\theta)^2 / 4$$

Where,

$$\gamma = 0.082 \text{ mN m}^{-1} \rightarrow \gamma = O(10^{-5}) \text{ N m}^{-1}$$

Considering the smallest particle size,

$$d = 1 \text{ }\mu\text{m} \rightarrow d = O(10^{-6}) \text{ m}$$

Considering the largest particle size,

$$d = 10 \text{ }\mu\text{m} \rightarrow d = O(10^{-5}) \text{ m}$$

$$\theta = 90 \text{ }^\circ\text{C}$$

Therefore, the order-of-magnitude approximation can be calculated as the following

Smallest particle size:

$$\Delta G = \gamma d^2 (1 - \cos\theta)^2 / 4$$

$$\Delta G = O(10^{-5}) O(10^{-12}) O(10^{-1}) = O(10^{-18}) \text{ J}$$

Largest particle size:

$$\Delta G = \gamma d^2 (1 - \cos\theta)^2 / 4$$

$$\Delta G = O(10^{-5}) O(10^{-10}) O(10^{-1}) = O(10^{-16}) \text{ J}$$

## Thermal energy

The Gibbs desorption free energy can be found by the following:

$$kT$$

Where,

$$k = 1.38 \times 10^{-23} \text{ m}^2 \text{ kg s}^{-2} \text{ K}^{-1} \rightarrow k = O(10^{-23}) \text{ m}^2 \text{ kg s}^{-2} \text{ K}^{-1}$$

$$T = 293.15 \text{ K} \rightarrow T = O(10^2) \text{ K}$$

Therefore, the order-of-magnitude approximation can be calculated as the following:

$$kT = O(10^{-23}) O(10^2) = O(10^{-21}) \text{ J}$$

## Stokes' drag-based shear energy

The Stokes' drag –based shear energy can be found as the following:

$$6\pi\mu_{PEG}udD/2$$

Where,

$$\mu_{PEG} = 15.0 \text{ mPa s} \rightarrow \mu_{PEG} = O(10^{-2}) \text{ Pa s}$$

$$u = 6.1 \text{ } \mu\text{m s}^{-1} \rightarrow u = O(10^{-6}) \text{ m s}^{-1}$$

Considering the smallest particle size,

$$d = 1 \text{ } \mu\text{m} \rightarrow d = O(10^{-6}) \text{ m}$$

Considering the largest particle size,

$$d = 10 \text{ } \mu\text{m} \rightarrow d = O(10^{-5}) \text{ m}$$

$$D = 50 \text{ } \mu\text{m} \rightarrow D = O(10^{-5}) \text{ m}$$

Therefore, the order-of-magnitude approximation can be calculated as the following

Smallest particle size:

$$6\pi\mu_{PEG}udD/2 = O(10^1) O(10^{-2}) O(10^{-6}) O(10^{-6}) O(10^{-5}) = O(10^{-18})$$

Largest particle size:

$$6\pi\mu_{PEG}udD/2 = O(10^1) O(10^{-2}) O(10^{-6}) O(10^{-5}) O(10^{-5}) = O(10^{-17})$$

# Bibliography

- 1 G. M. Whitesides, *Nature*, 2006, **442**, 368–373.
- 2 E. K. Sackmann, A. L. Fulton and D. J. Beebe, *Nature*, 2014, **507**, 181–189.
- 3 Y. Xia and G. M. Whitesides, *Annu. Rev. Mater. Sci.*, 1998, **28**, 153–184.
- 4 D. B. Weibel and G. M. Whitesides, *Curr. Opin. Chem. Biol.*, 2006, **10**, 584–591.
- 5 C. Yi, C.-W. Li, S. Ji and M. Yang, *Anal. Chim. Acta*, 2006, **560**, 1–23.
- 6 R. Daw and J. Finkelstein, *Nature*, 2006, **442**, 367.
- 7 L. Van Heirstraeten, P. Spang, C. Schwind, K. S. Drese, M. Ritzi-Lehnert, B. Nieto, M. Camps, B. Landgraf, F. Guasch, A. H. Corbera, J. Samitier, H. Goossens, S. Malhotra-Kumar and T. Roeser, *Lab Chip*, 2014, **14**, 1519–1526.
- 8 G. G. Nestorova, K. Hasenstein, N. Nguyen, M. A. DeCoster and N. D. Crews, *Lab Chip*, 2017, **17**, 1128–1136.
- 9 C. H. Ahn, J.-W. Choi, G. Beaucage, J. H. Nevin, J.-B. Lee, A. Puntambekar and J. Y. Lee, *Proc. IEEE*, 2004, **92**, 154–173.
- 10 V. Srinivasan, V. K. Pamula and R. B. Fair, *Lab Chip*, 2004, **4**, 310–315.
- 11 C. Hu, G. Munglani, H. Vogler, T. Ndinyanka Fabrice, N. Shamsudhin, F. K. Wittel, C. Ringli, U. Grossniklaus, H. J. Herrmann and B. J. Nelson, *Lab Chip*, 2017, **17**, 82–90.
- 12 D. A. Lawson, N. R. Bhakta, K. Kessenbrock, K. D. Prummel, Y. Yu, K. Takai, A. Zhou, H. Eyob, S. Balakrishnan, C. Y. Wang, P. Yaswen, A. Goga and Z. Werb, *Nature*, 2015, **526**, 131–135.
- 13 D. J. Beebe, G. A. Mensing and G. M. Walker, *Annu. Rev. Biomed. Eng.*, 2002, **4**, 261–286.
- 14 H. A. Stone and S. Kim, *AIChE J.*, 2001, **47**, 1250–1254.
- 15 K. Ohno, K. Tachikawa and A. Manz, *Electrophoresis*, 2008, **29**, 4443–4453.
- 16 T. M. Squires and S. R. Quake, *Rev. Mod. Phys.*, 2005, **77**, 977–1026.
- 17 J. Atencia and D. J. Beebe, *Nature*, 2005, **437**, 648–655.

- 18 S.-Y. Teh, R. Lin, L.-H. Hung and A. P. Lee, *Lab Chip*, 2008, **8**, 198–220.
- 19 L. Rosenfeld, T. Lin, R. Derda and S. K. Y. Tang, *Microfluid. Nanofluidics*, 2014, **16**, 921–939.
- 20 T. S. Kaminski, O. Scheler and P. Garstecki, *Lab Chip*, 2016, **16**, 2168–2187.
- 21 T. Thorsen, R. W. Roberts, F. H. Arnold and S. R. Quake, *Phys. Rev. Lett.*, 2001, **86**, 4163–4166.
- 22 T. Nisisako, T. Torii and T. Higuchi, *Lab Chip*, 2002, **2**, 24–26.
- 23 J. D. Tice, H. Song, A. D. Lyon and R. F. Ismagilov, *Langmuir*, 2003, **19**, 9127–9133.
- 24 S. L. Anna, N. Bontoux and H. A. Stone, *Appl. Phys. Lett.*, 2003, **82**, 364–366.
- 25 L. Yobas, S. Martens, W.-L. Ong and N. Ranganathan, *Lab Chip*, 2006, **6**, 1073–1079.
- 26 J. Hogan, *Nature*, 2006, **442**, 351–352.
- 27 G. T. Roman, Y. Chen, P. Viberg, A. H. Culbertson and C. T. Culbertson, *Anal. Bioanal. Chem.*, 2007, **387**, 9–12.
- 28 H. N. Joensson and H. Andersson Svahn, *Angew. Rev.*, 2012, **51**, 12176–12192.
- 29 E. Brouzes, M. Medkova, N. Savenelli, D. Marran, M. Twardowski, J. B. Hutchison, J. onatha. M. Rothberg, D. R. Link, N. Perrimon and M. L. Samuels, *Proc. Natl. Acad. Sci.*, 2009, **106**, 14195–14200.
- 30 M. Weiss, J. P. Frohnmayer, L. T. Benk, B. Haller, J. W. Janiesch, T. Heitkamp, M. Börsch, R. B. Lira, R. Dimova, R. Lipowsky, E. Bodenschatz, J. C. Baret, T. Vidakovic-Koch, K. Sundmacher, I. Platzman and J. P. Spatz, *Nat. Mater.*, 2018, **17**, 89–95.
- 31 Y. Elani, T. Trantidou, D. Wylie, L. Dekker, K. Polizzi, R. V. Law and O. Ces, *Sci. Rep.*, 2018, **8**, 1–8.
- 32 D. A. LaVan, T. McGuire and R. Langer, *Nat. Biotechnol.*, 2003, **21**, 1184–1191.
- 33 P. M. Valencia, O. C. Farokhzad, R. Karnik and R. Langer, *Nat. Nanotechnol.*, 2012, **7**, 623–629.
- 34 K. S. Huang, T. H. Lai and Y. C. Lin, *Lab Chip*, 2006, **6**, 954–957.
- 35 H. C. Shum, A. R. Abate, D. Lee, A. R. Studart, B. Wang, C.-H. Chen, J. Thiele, R. K. Shah, A. Krummel and D. A. Weitz, *Macromol. Rapid Commun.*, 2010, **31**, 108–118.
- 36 T. Nisisako and T. Torii, *Adv. Mater.*, 2007, **19**, 1489–1493.
- 37 M. B. Romanowsky, A. R. Abate, A. Rotem, C. Holtze and D. A. Weitz, *Lab Chip*, 2012,

- 12, 802–807.
- 38 M. L. J. Steegmans, A. Warmerdam, K. G. P. H. Schroen and R. M. Boom, *Langmuir*, 2009, **25**, 9751–9758.
- 39 Y. Chevalier and M. A. Bolzinger, *Colloids Surfaces A Physicochem. Eng. Asp.*, 2013, **439**, 23–34.
- 40 H. Zhang, E. Tumarkin, R. M. A. Sullan, G. C. Walker and E. Kumacheva, *Macromol. Rapid Commun.*, 2007, **28**, 527–538.
- 41 S. Sugiura, T. Oda, Y. Izumida, Y. Aoyagi, M. Satake, A. Ochiai, N. Ohkohchi and M. Nakajima, *Biomaterials*, 2005, **26**, 3327–3331.
- 42 F. Ikkai, S. Iwamoto, E. Adachi and M. Nakajima, *Colloid Polym. Sci.*, 2005, **283**, 1149–1153.
- 43 H. Huang, Y. Yu, Y. Hu, X. He, O. B. Usta and M. L. Yarmush, *Lab Chip*, 2017, **17**, 1913–1932.
- 44 Y. Deng, N. Zhang, L. Zhao, X. Yu, X. Ji, W. Liu, S. Guo, K. Liu and X. Z. Zhao, *Lab Chip*, 2011, **11**, 4117–4121.
- 45 S. Hong, H. J. Hsu, R. Kaunas and J. Kameoka, *Lab Chip*, 2012, **12**, 3277–3280.
- 46 R. S. King, H. W. Blanch and J. M. Prausnitz, *AIChE J.*, 1988, **34**, 1585–1594.
- 47 S. Hardt and T. Hahn, *Lab Chip*, 2012, **12**, 434–42.
- 48 M. Tsukamoto, S. Taira, S. Yamamura, Y. Morita, N. Nagatani, Y. Takamura and E. Tamiya, *Analyst*, 2009, **134**, 1994–1998.
- 49 P.-A. Albertsson and E. J. Nyns, *Nature*, 1959, **84**, 1465–1468.
- 50 B. A. Andrews, A. S. Schmidt and J. A. Asenjo, *Biotechnol. Bioeng.*, 2005, **90**, 380–390.
- 51 E. Eriksson, P. Å. Albertsson and G. Johansson, *Mol. Cell. Biochem.*, 1976, **10**, 123–128.
- 52 D. M. Brunette and J. E. Till, *J. Membr. Biol.*, 1971, **5**, 215–224.
- 53 P.-A. Albertsson, A. Cajarville, D. E. Brooks and F. Tjerneld, *Biochim. Biophys. Acta*, 1987, **926**, 87–93.
- 54 P.-Å. Albertsson, *Biochemistry*, 1973, **12**, 2525–2530.
- 55 W. Ramsden, *Proc. R. Soc. L.*, 1903, **72**, 156–164.
- 56 S. U. Pickering, *J. Chem. Soc. Trans.*, 1907, **91**, 2001–2021.
- 57 S. Simovic and C. A. Prestidge, *J. Drug Deliv. Sci. Technol.*, 2011, **21**, 123–133.

- 58 J. Frelichowska, M. A. Bolzinger, J. P. Valour, H. Mouaziz, J. Pelletier and Y. Chevalier, *Int. J. Pharm.*, 2009, **368**, 7–15.
- 59 J. Frelichowska, M. A. Bolzinger, J. Pelletier, J. P. Valour and Y. Chevalier, *Int. J. Pharm.*, 2009, **371**, 56–63.
- 60 A. D. Dinsmore, M. F. Hsu, M. G. Nikolaidis, M. Marquez, A. R. Bausch and D. A. Weitz, *Science (80-. )*, 2002, **298**, 1006–1009.
- 61 D. Lee and D. A. Weitz, *Small*, 2009, **5**, 1932–1935.
- 62 B. P. Binks, *Adv. Mater.*, 2002, **14**, 1824–1827.
- 63 J. Zhou, X. Qiao, B. P. Binks, K. Sun, M. Bai, Y. Li and Y. Liu, *Langmuir*, 2011, **27**, 3308–3316.
- 64 J. W. J. de Folter, M. W. M. van Ruijven and K. P. Velikov, *Soft Matter*, 2012, **8**, 6807–6815.
- 65 E. Vignati, R. Piazza and T. P. Lockhart, *Langmuir*, 2003, **19**, 6650–6656.
- 66 B. P. Binks and S. O. Lumsdon, *Langmuir*, 2001, **17**, 4540–4547.
- 67 H. A. Wege, S. Kim, V. N. Paunov, Q. Zhong and O. D. Velev, *Langmuir*, 2008, **24**, 9245–9253.
- 68 A. Huebner, S. Sharma, M. Srisa-Art, F. Hollfelder, J. B. Edel and A. J. DeMello, *Lab Chip*, 2008, **8**, 1244–1254.
- 69 W. Wang, M. J. Zhang and L. Y. Chu, *Acc. Chem. Res.*, 2014, **47**, 373–384.
- 70 Z. Nie, J. I. Park, W. Li, S. A. F. Bon and E. Kumacheva, *J. Am. Chem. Soc.*, 2008, **130**, 16508–16509.
- 71 C. Priest, M. D. Reid and C. P. Whitby, *J. Colloid Interface Sci.*, 2011, **363**, 301–306.
- 72 A. B. Subramaniam, M. Abkarian and H. A. Stone, *Nat. Mater.*, 2005, **4**, 553–556.
- 73 A. T. Poortinga, *Langmuir*, 2008, **24**, 1644–1647.
- 74 P.-A. Albertsson, *Nature*, 1956, **177**, 771–774.
- 75 S. Hardt and T. Hahn, *Lab Chip*, 2012, **12**, 434–442.
- 76 A. L. Grilo, M. R. Aires-Barros and A. M. Azevedo, *Sep. Purif. Rev.*, 2016, **45**, 68–80.
- 77 Y. Song, Y. K. Chan, Q. Ma, Z. Liu and H. C. Shum, *ACS Appl. Mater. Interfaces*, 2015, **7**, 13925–13933.
- 78 C. Han, S. Takayama and J. Park, *Sci. Rep.*, 2015, **5**, 1–11.

- 79 S. D. Geschiere, I. Ziemecka, V. van Steijn, G. J. M. Koper, J. H. van Esch and M. T. Kreutzer, *Biomicrofluidics*, 2012, **6**, 022007-1–11.
- 80 L. Shang, Y. Cheng and Y. Zhao, *Chem. Rev.*, 2017, **117**, 7964–8040.
- 81 Y. S. Song, Y. H. Choi and D. H. Kim, *J. Chromatogr. A*, 2007, **1162**, 180–186.
- 82 I. Ziemecka, V. van Steijn, G. J. M. Koper, M. Rosso, A. M. Brizard, J. H. van Esch and M. T. Kreutzer, *Lab Chip*, 2011, **11**, 620–624.
- 83 D. Lai, J. P. Frampton, H. Sriram and S. Takayama, *Lab Chip*, 2011, **11**, 3551–3554.
- 84 H. C. Shum, J. Varnell and D. A. Weitz, *Biomicrofluidics*, 2012, **6**, 012808-1–9.
- 85 B. Moon, S. G. Jones, D. K. Hwang and S. S. H. Tsai, *Lab Chip*, 2015, **15**, 2437–2444.
- 86 B. Moon, N. Abbasi, S. G. Jones, D. K. Hwang and S. S. H. Tsai, *Anal. Chem.*, 2016, **88**, 3982–3989.
- 87 G. Balakrishnan, T. Nicolai, L. Benyahia and D. Durand, *Langmuir*, 2012, **28**, 5921–5926.
- 88 B. T. Nguyen, T. Nicolai and L. Benyahia, *Langmuir*, 2013, **29**, 10658–10664.
- 89 E. Atefi, J. A. Mann and H. Tavana, *Langmuir*, 2014, **30**, 9691–9699.
- 90 S. G. Jones, N. Abbasi, B.-U. Moon and S. S. H. Tsai, *Soft Matter*, 2016, **12**, 2668–2675.
- 91 H. Firoozmand, B. S. Murray and E. Dickinson, *Langmuir*, 2009, **25**, 1300–1305.
- 92 P. G. Saffman, *J. Fluid Mech.*, 1965, **22**, 385–400.
- 93 E. C. Mbamala and H. H. Von Grünberg, *J. Phys. Condens. Matter*, 2002, **14**, 4881–4900.
- 94 K. Arnold, A. Herrmann, L. Pratsch and K. Gawrisch, *Biochim. Biophys. Acta - Biomembr.*, 1985, **815**, 515–518.
- 95 B. Y. Zaslavsky, L. M. Miheeva, M. N. Rodnikova, G. V. Spivak, V. S. Harkin and A. U. Mahmudov, *J. Chem. Soc. Faraday Trans. 1 Phys. Chem. Condens. Phases*, 1989, **85**, 2857–2865.
- 96 V. K. La Mer and T. W. Healy, *J. Phys. Chem.*, 1963, **67**, 2417–2420.
- 97 R. Gref, Y. Minamitake, M. T. Peracchia, V. Trubetskoy, V. Torchilin and R. Langer, *Science (80-. )*, 1994, **263**, 1600–1603.
- 98 S. Mitragotri and J. Lahann, *Nat. Mater.*, 2009, **8**, 15–23.
- 99 J. A. Champion, Y. K. Katare and S. Mitragotri, *J. Control. Release*, 2007, **121**, 3–9.
- 100 J. M. Anderson and M. S. Shive, *Adv. Drug Deliv. Rev.*, 1997, **28**, 5–24.
- 101 S. Stolnik, L. Illum and S. S. Davis, *Adv. Drug Deliv. Rev.*, 1995, **16**, 195–214.

- 102 G. Storn, S. O. Beliot, T. Daemen and D. D. Lasic, *Adv. Drug Deliv. Rev.*, 1995, **17**, 31–48.
- 103 O. Pillai and R. Panchagnula, *Curr. Opin. Chem. Biol.*, 2001, **5**, 447–451.
- 104 A. Smith and I. M. Hunneyball, *Int. J. Pharm.*, 1986, **30**, 215–220.
- 105 B. Conti, F. Pavanetto and I. Genta, *J. Microencapsul.*, 1992, **9**, 153–166.
- 106 J. P. Rolland, B. W. Maynor, L. E. Euliss, A. E. Exner, G. M. Denison and J. M. DeSimone, *J. Am. Chem. Soc.*, 2005, **127**, 10096–10100.
- 107 F. Rancan, D. Papakostas, S. Hadam, S. Hackbarth, T. Delair, C. Primard, B. Verrier, W. Sterry, U. Blume-Peytavi and A. Vogt, *Pharm. Res.*, 2009, **26**, 2027–2036.
- 108 K. Lee, K. R. Yoon, S. I. Woo and I. S. Choi, *J. Pharm. Sci.*, 2003, **92**, 933–937.
- 109 H. Gupta, M. Aqil, R. K. Khar, A. Ali, A. Bhatnagar and G. Mittal, *Nanomedicine Nanotechnology, Biol. Med.*, 2010, **6**, 324–333.
- 110 B. Semete, L. Booyesen, Y. Lemmer, L. Kalombo, L. Katata, J. Verschoor and H. S. Swai, *Nanomedicine Nanotechnology, Biol. Med.*, 2010, **6**, 662–671.
- 111 J. Zhang, S. Rana, R. S. Srivastava and R. D. K. Misra, *Acta Biomater.*, 2008, **4**, 40–48.
- 112 A. Lavasanifar, J. Samuel and G. S. Kwon, *Adv. Drug Deliv. Rev.*, 2002, **54**, 169–190.
- 113 A. Apicella, B. Cappello, M. A. Del Nobile, M. I. La Rotonda, G. Mensitieri and L. Nicolais, *Biomaterials*, 1993, **14**, 83–90.
- 114 H.-C. Chiu, G.-H. Hsiue, Y.-P. Lee and L.-W. Huang, *J. Biomater. Sci. Polym. Ed.*, 1999, **10**, 591–608.
- 115 R. Cortesi, E. Esposito, M. Osti, G. Squarzone, E. Menegatti, S. S. Davis and C. Nastruzzi, *Eur. J. Pharm. Biopharm.*, 1999, **47**, 153–160.
- 116 L. Hovgaard and H. Brndsted, 1995, **36**, 159–166.
- 117 M. Dunne, O. I. Corrigan and Z. Ramtoola, *Biomaterials*, 2000, **21**, 1659–1668.
- 118 V. R. S. Patil, C. J. Campbell, Y. H. Yun, S. M. Slack and D. J. Goetz, *Biophys. J.*, 2001, **80**, 1733–1743.
- 119 J. A. Champion, A. Walker and S. Mitragotri, *Pharm. Res.*, 2008, **25**, 1815–1821.
- 120 R. C. Mundargi, M. G. Potroz, S. Park, H. Shirahama, J. H. Lee, J. Seo and N.-J. Cho, *Small*, 2016, **12**, 1167–1173.
- 121 S. E. A. Gratton, P. A. Ropp, P. D. Pohlhaus, J. C. Luft, V. J. Madden, M. E. Napier and J.

- M. DeSimone, *Proc. Natl. Acad. Sci.*, 2008, **105**, 11613–11618.
- 122 Y. Hennequin, N. Pannacci, C. P. De Torres, G. Tetradis-Meris, S. Chapuliot, E. Bouchaud and P. Tabeling, *Langmuir*, 2009, **25**, 7857–7861.
- 123 Y. Hu, Q. Wang, J. Wang, J. Zhu, H. Wang and Y. Yang, *Biomicrofluidics*, 2012, **6**, 1–9.
- 124 M. Hussain, J. Xie, Z. Hou, K. Shezad, J. Xu, K. Wang, Y. Gao, L. Shen and J. Zhu, *ACS Appl. Mater. Interfaces*, 2017, **9**, 14391–14400.
- 125 C. Yu, M. Xu, F. Svec and J. M. J. Frechet, *J. Polym. Sci. Part A Polym. Chem.*, 2002, **40**, 755–769.
- 126 Z. Nie, S. Xu, M. Seo, P. C. Lewis and E. Kumacheva, *J. Am. Chem. Soc.*, 2005, **127**, 8058–8063.
- 127 D. K. Hwang, D. Dendukuri and P. S. Doyle, *Lab Chip*, 2008, **8**, 1640–1647.
- 128 L. C. Glangchai, M. Caldorera-Moore, L. Shi and K. Roy, *J. Control. Release*, 2008, **125**, 263–272.
- 129 D. Dendukuri, D. C. Pregibon, J. Collins, T. A. Hatton and P. S. Doyle, *Nat. Mater.*, 2006, **5**, 365–369.
- 130 D. Dendukuri, T. A. Hatton and P. S. Doyle, *Langmuir*, 2007, **23**, 4669–4674.
- 131 K. Choi, M. Salehizadeh, R. B. Da Silva, N. Hakimi, E. Diller and D. K. Hwang, *Soft Matter*, 2017, **13**, 7255–7263.
- 132 D. An, A. Warning, K. G. Yancey, C. T. Chang, V. R. Kern, A. K. Datta, P. H. Steen, D. Luo and M. Ma, *Nat. Commun.*, 2016, **7**, 1–10.
- 133 M. Jeyhani, S. Y. Mak, S. Sammut, H. C. Shum, D. K. Hwang and S. S. H. Tsai, *ChemPhysChem*, 2018, **19**, 1–7.
- 134 A. Diego-Taboada, S. T. Beckett, S. L. Atkin and G. Mackenzie, *Pharmaceutics*, 2014, **6**, 80–96.
- 135 B. P. Binks, A. N. Boa, M. A. Kibble, G. MacKenzie and A. Rocher, *Soft Matter*, 2011, **7**, 4017–4024.
- 136 W. Brandon Goodwin, I. J. Gomez, Y. Fang, J. C. Meredith and K. H. Sandhage, *Chem. Mater.*, 2013, **25**, 4529–4536.
- 137 F. Cao and D. X. Li, *Biomed. Mater.*, 2009, **4**, 1–6.
- 138 S. R. Hall, H. Bolger and S. Mann, *Chem. Commun.*, 2003, **3**, 2784–2785.

- 139 A. Einstein, *Ann. Phys.*, 1905, **322**, 549–560.
- 140 V. Gnyawali, M. Saremi, M. C. Kolios and S. S. H. Tsai, *Biomicrofluidics*, 2017, **11**, 1–7.
- 141 K. L. Thompson, S. P. Armes and D. W. York, *Langmuir*, 2011, **27**, 2357–2363.

